

# Synthesis-driven design of 3D molecules for structure-based drug discovery using geometric transformers

Yibo Li,<sup>†</sup> Jianfeng Pei,<sup>\*,‡</sup> and Luhua Lai<sup>\*,†,‡,¶</sup>

<sup>†</sup> *Center for Life Sciences, Academy for Advanced Interdisciplinary Studies, Peking University, Beijing 100871, China*

<sup>‡</sup> *Center for Quantitative Biology, Academy for Advanced Interdisciplinary Studies, Peking University, Beijing 100871, China*

<sup>¶</sup> *BNLMS, College of Chemistry and Molecular Engineering, Peking University, Beijing 100871, China*

E-mail: jfpei@pku.edu.cn; lhlai@pku.edu.cn

## Abstract

Finding drug-like compounds with high bioactivity is essential for drug discovery, but the task is complicated by the high cost of chemical synthesis and validation. With their outstanding performance in *de novo* drug design, deep generative models represent promising tools for tackling this challenge. In recently years, 3D molecule generative models have gained increasing attention due to their ability to directly utilize the 3D interaction information between the target and ligand. However, it remains challenging to synthesize the molecules generated by these models, limiting the speed of bioactivity validation and further structure optimization. In this work, we propose DeepLigBuilder+, a deep generative model for 3D molecules that combines structure-based *de novo* drug

design with a reaction-based generation framework. Besides producing 3D molecular structures, the model also proposes synthetic pathways for generated molecules, which greatly assists the retro-synthetic analysis. To achieve this, we developed a new way to enforce the synthesizability constraint using a tree-based organization of purchasable building blocks. This method enjoys high scalability and is compatible with existing atom-based generative models. Additionally, for structure-based design tasks, we developed an SE(3)-equivariant transformer conditioned on the shape and pharmacophore-based inputs, and combine it with the Monte Carlo tree search. Using the ATP-binding pocket of BTK and the NAD<sup>+</sup> binding pocket of PHGDH for case studies, we demonstrate that DeepLigBuilder+ is capable of enriching drug-like molecules with high predicted binding affinity and desirable interaction modes while maintaining the synthesizability constraint. We believe that DeepLigBuilder+ is a powerful tool for accelerating the process of drug discovery, and represents an important step towards a fully automated design-synthesis-evaluation workflow for molecule design.

## 1 Introduction

The high financial cost and low success rate of drug discovery place tremendous challenges in finding treatments for important diseases.<sup>1</sup> To address those challenges, computational methods have been developed to find promising compounds from the vast space of chemical structures for subsequent biological validation. Computational virtual screening (VS) have been widely used, which filters chemical libraries using scoring functions<sup>2</sup> for favorable compounds. In spite of their success in finding bioactive molecules,<sup>3</sup> VS is constrained by the screening library it uses. Small libraries may have limited coverage of the chemical space, and large ones impose high computational costs for the screening process and require specialized software and hardware platforms.<sup>4</sup> *De novo* drug design, which uses computational algorithms to generate molecule structures from scratch,<sup>5</sup> provides an option to explore new

chemical space beyond libraries of existing compounds.

Over the decades, a variety of *de novo* drug design programs have been proposed, such as LEGEND,<sup>6</sup> LUDI,<sup>7</sup> CONCEPTS<sup>8</sup> and LigBuilder,<sup>9-11</sup> many of which have been used to design bioactive molecules with successful experimental validation.<sup>12-16</sup>

In recent years, deep molecule generative models have emerged as a new class of promising methods for *de novo* drug design.<sup>17</sup> Using deep learning, models can automatically learn traits of desirable molecule structures from the training data, with little need for manual intervention. This contrasts significantly with traditional *de novo* design programs, which in general require extensive efforts to design the search rules and scoring functions. The advantages of deep generative models have helped to spawn a series of research aiming to utilize them for drug discovery. Those works range from exploring different molecule representations, including SMILES<sup>18</sup> and molecular graph,<sup>19-21</sup> to testing with various training methods, such as VAE,<sup>22</sup> GAN<sup>23,24</sup> and RL.<sup>25,26</sup> As a result, a wide range of models has been proposed to address various issues related to drug design based on molecular properties,<sup>22</sup> pharmacophores,<sup>27</sup> scaffolds<sup>28</sup> and targets.<sup>29</sup>

Most deep generative models for molecules have been focused on designing the 2D (topological) chemical structures, but the foundation of bioactivity lies in the interactions between the 3D structures of targets and ligands. Directly generating 3D molecules inside the target binding pocket can help the model to better utilize the interaction information. Additionally, it can reduce the need for ligand-based information, potentially leading to molecules with higher novelty. Those benefits have led to growing attention in developing 3D generative models of molecules based on target information. Earlier approaches include models that convert 3D pocket information into SMILES strings, such as LiGANN<sup>30</sup> and the pocket-conditioned RNN proposed by Xu et al.,<sup>31</sup> but the generated structure only contains topological information. In order to directly generate 3D structures, Masuda et al.<sup>32</sup> proposed liGAN, which uses VAE based on 3D-CNN to generate atomic density grids, and later convert the grids to 3D molecules. To avoid the conversion between different represen-

tations, we previously proposed DeepLigBuilder<sup>33</sup> to directly produce 3D molecules inside pockets using graph generative models and Monte Carlo tree search. Other graph generative models, such as Pocket2Mol,<sup>34</sup> use equivariant networks to encode pocket information as conditional inputs. More recent works have experimented with diffusion models for 3D molecule generation, such as DiffLinker,<sup>35</sup> which features a permutation invariant way of generation compared to autoregressive models.

Despite progress in structure-based 3D deep generative models, there is still a critical issue to be addressed: the synthesizability of generated molecules. Chemical synthesis is a common rate-limiting step in medicinal chemistry research. Since *de novo* design programs are not constrained by any compound library, it is easier for these methods to propose molecules that are challenging to synthesize, especially in objective-directed situations,<sup>36</sup> making experimental validation difficult. A solution to this problem is to use synthetically aware models.<sup>37</sup> Those models generate molecules by generating their synthetic path, using explicit building blocks and chemical reactions. Such approaches have been relatively common in traditional *de novo* design programs, such as SYNOPSIS<sup>38</sup> and DOGS,<sup>39</sup> but is largely absent from early deep learning methods. More recently, an increasing number of models have been proposed to integrate this approach with deep generative networks, including MoleculeChef,<sup>40</sup> DoG-AE and DoG-Gen,<sup>41</sup> PGFS<sup>42</sup> and SynNet.<sup>43</sup> Those methods have shown promising results, but they are largely focused on 2D molecule design, which, as discussed before, inherits several limitations compared to recent 3D generative models. Based on the discussions above, we believe that it is highly beneficial to develop a deep generative model that can perform pocket-based 3D molecule design while ensuring the synthesizability of the generated molecules. In this work, we combine geometric deep learning and synthesizability constraints to develop a new *de novo* drug design program, DeepLigBuilder+. The program follows a reaction-based scheme for generating drug-like molecules, while at the same time produces their 3D conformations, making it easy to be applied to structure-based design tasks. Specifically, we use a transformer network to generate 3D molecular graphs

atom-by-atom, while at each step, we mask inappropriate atom and bond types from the action space so that the output structure is guaranteed to be inside the user-provided reactant dataset (represented as synthons). In order to incorporate 3D pocket information, we trained an SE(3)-equivariant transformer network conditioned on pharmacophore and shape information, and combine it with a reinforcement learning module based on Monte Carlo tree search (MCTS). To demonstrate the capability of DeepLigBuilder+ in drug design applications, we use it to design inhibitors targeting the ATP-binding pocket of Bruton’s tyrosine kinase (BTK), as well as the NAD<sup>+</sup>-binding pocket of human phosphoglycerate dehydrogenase (PHGDH). In both cases, DeepLigBuilder+ generated molecules with high predicted binding affinity and favorable binding modes while maintaining the enforced synthesizability constraint.

## 2 Methods

In this section, we give a brief account of the architecture of DeepLigBuilder+. The implementation details for DeepLigBuilder+ are provided in the Supplementary Methods (Section S1).

To ensure high synthetic accessibility, DeepLigBuilder+ generates molecules one reactant at a time and then produces the resulting molecules using corresponding reaction rules. Unlike previous methods, DeepLigBuilder+ also generates 3D conformation of the molecule for subsequent structure-based design tasks. Since many reactions involve large conformational changes, instead of directly generating 3D structures of reactants, DeepLigBuilder+ first generates synthon structures and later convert them to the corresponding reactants, as shown in Figure 1a and g. Synthons are hypothetical reactants that have one or more open valences with specific reactivity. A reactant can be converted to a synthon by extracting the substructure of the product that is derived from this reactant. In this way, adding a new synthon to the molecule will not affect the conformation of previous synthons, making

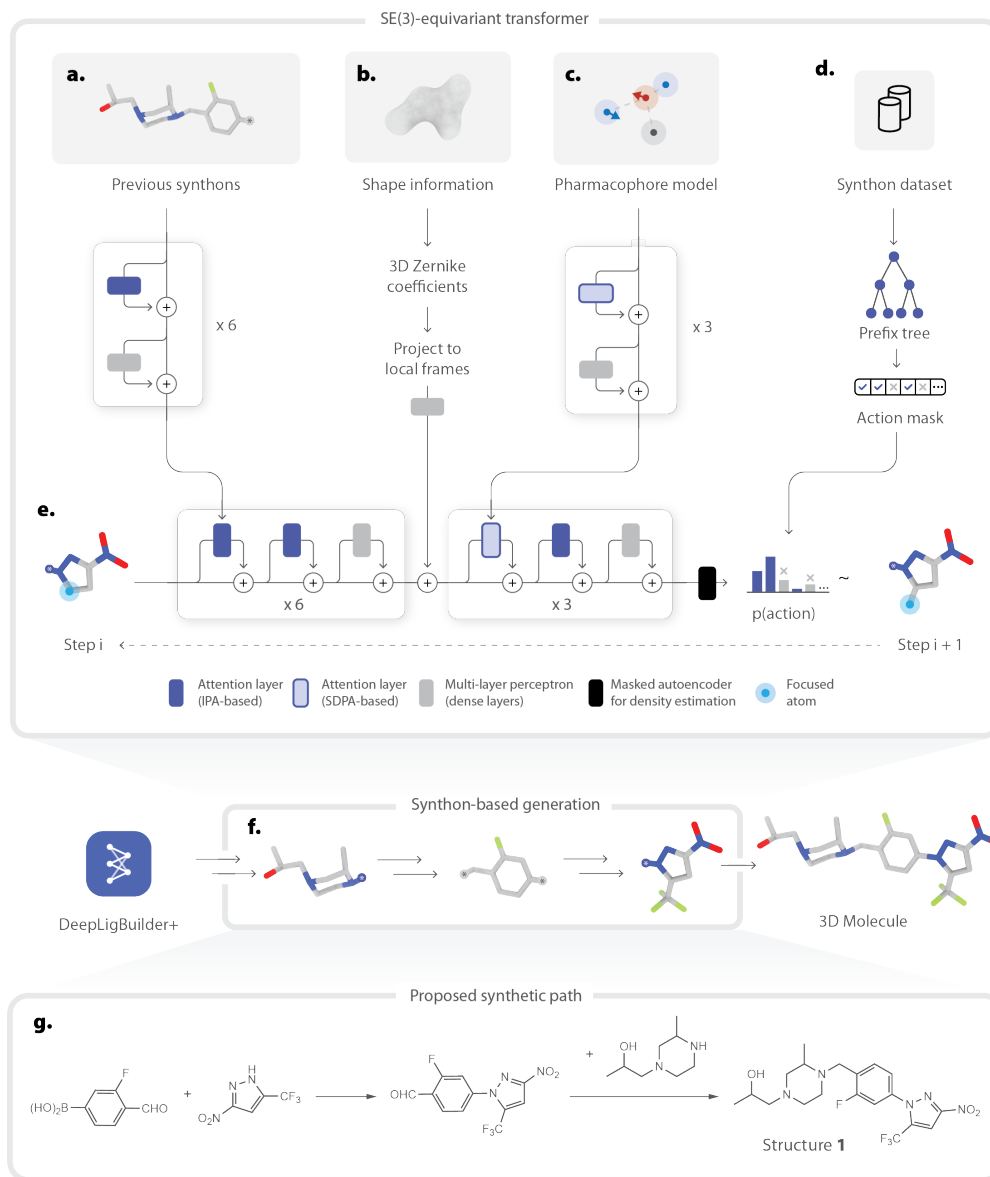


Figure 1: An overview of DeepLigBuilder+. It generates synthesizable 3D molecules following a reaction-based method using synthons (f). When producing each synthon, the model adopts a graph-based generation scheme (e) that iteratively edits the molecular graph by adding new nodes (atoms) or edges (bonds). The decisions of how to perform those edits are made by a transformer network (a-e). The encoders are used to process the input information, such as previously generated synthons (a). For structure-based generation tasks, the encoder also receives shape(b) and pharmacophore(c)-based inputs. The decoder (e) uses those input information to produce a state embedding, which is later used by the policy network (based on MADE blocks) to output a distribution in the action space. We apply action masks at each step to constrain the generation trajectory so that it only produces synthons that can be converted into purchasable building blocks (d). Finally, the generated synthons can be converted to a synthetic route, with explicit reactants and reaction types (g).

it more suitable for 3D generation tasks. In this work, we use the global stock of Enamine building blocks as the reactant set and use the reactions collected by Hartenfeller et al.<sup>44</sup>. Each product molecule is assembled from three reactants using two reaction steps. Details related to the synthon dataset are given in Section S1.1.

When generating each synthon structure, we adopt a graph-based approach similar to our previous work.<sup>33</sup> Specifically, we treat the synthon structure as a 3D graph, and it is generated by iteratively refining the graph structure. At each step, the model either adds a new atom or a new bond or performs other operations such as backtracking. We also introduce various improvements compared to the previous method, including a more detailed treatment of ring generation. Specifically, before generating each ring structure, DeepLigBuilder+ first specify the size of the ring, as well as the location the ring will be closed. This can better guide the generation process and can avoid potential issues when the user changes the synthon dataset (see Figure S5). The generation scheme is detailed in Section S1.2.

During generation, we need to constrain the synthon structure to the space of purchasable building blocks. To achieve this, we perform step-wise masking of the action space so that the generated structure will not leave the space of purchasable synthons. The mask is constructed by querying a prefix tree of synthon structures built from the building block dataset, as detailed in Section S1.3. This new method of introducing chemical constraints offers better scalability compared to previous approaches,<sup>41,43</sup> which usually requires a scan through the entire set of building blocks to generate the next action.

DeepLigBuilder+ uses an SE(3) equivariant transformer to decide which action to perform at each step of generation. Specifically, we convert a 3D molecular graph as a sequence of actions that are used to generate its structure. This is equivalent to the concept of a "sentence" in NLP-related tasks. Correspondingly, each action represents a "word" in the sentence. The network adopts an encoder-decoder architecture, which is used to translate the input information, including previously generated synthons and pharmacophores (discussed

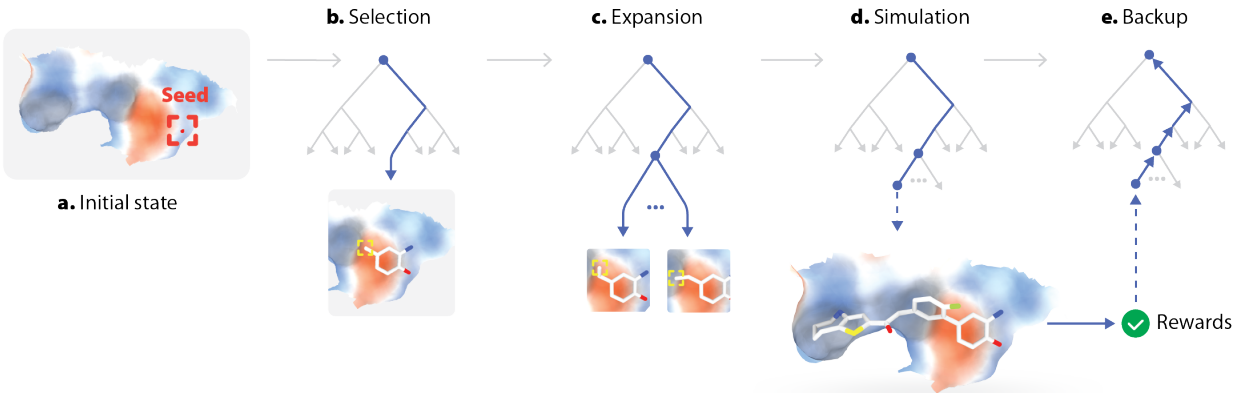


Figure 2: DeepLigBuilder+ uses Monte Carlo tree search (MCTS) to achieve structure-based molecule generation given the pocket structure. The search starts from a user-provided seed atom (a). In this figure, we use the ATP-binding pocket of BTK as an example. At each step, the model first selects a promising node from the look-ahead tree (b), then expands the tree by enumerating possible actions that can be performed on the 3D molecule (c). Next, the model selects an expanded state and uses the conditional transformer to perform the rollout (d). Finally, the generated molecule is evaluated using the Smina score, and the reward is backpropagated to parent nodes to update the Q-value estimates (e).

below), into new synthon structures, as shown in Figure 1. To incorporate 3D information in an equivariant manner, we attach a 3D coordinate system to the focused atom after each action and use invariant point attention (IPA)<sup>45</sup> to communicate information between actions. We also use relative 3D positional encoding to express the spatial relationship between action pairs. For network training, we assemble a drug-like set of synthesizable molecules from the Enamine building blocks, and use the 3D structures of these molecules generated by RDKit to train the model. More information related to the network and its training are given in Section S1.4 and Section S1.5.

To introduce 3D information of targets, Monte Carlo tree search (MCTS), a widely used algorithm in reinforcement learning, is applied to optimize the molecule structure inside the pocket (Figure 2). We use a search method similar to MENTS,<sup>46</sup> with custom modifications described in Section S1.6, and a reward function based on the Smina score.<sup>47</sup> The generated 3D pose by DeepLigBuilder+ is directly used for scoring, eliminating the time-consuming docking step.



To enhance the performance of MCTS, we developed a pharmacophore and shape-conditioned transformer as its rollout policy. Pharmacophore models represent abstracted interaction patterns that can be used to explain the bioactivity of ligands and are widely used in computer-aided drug design.<sup>48</sup> Shape information can help the model by constraining the molecule to match the geometry of the pocket. Those information are coded using SE(3) equivariant representations discussed in Section S1.4. For model training, a dataset of pharmacophore-ligand pairs is created by aligning synthesizable 3D molecules to pharmacophore features extracted from PDBBind ligands (Section S1.5). The conditional rollout policy offers significant speed ups for MCTS search, as demonstrated in the following sections.

## 3 Results

### 3.1 Performance of the unconditional generative model

We first evaluate the performance of the transformer network in the unconditional setting, in a manner similar to our previous work.<sup>33</sup> Specifically, we investigate whether the model is capable of generating drug-like and synthesizable molecules with valid 3D structures. Several generated molecules by the network are shown in Figure S6. A visual inspection of these molecules reveal that they all adopt reasonable 3D conformations. Local geometries are correctly structured based on the hybridization state of their atomic environments. Neighbors of sp<sup>2</sup>-atoms are planarized, while that of sp<sup>3</sup>-atoms form tetrahedron structures. Also, the overall conformations generated are relaxed and contain no significant clashes. Those observations will be later confirmed using quantitative evaluation metrics (see Section 3.1.3).

DeepLigBuilder+ is unique in that synthetic paths are also generated for each molecule along with its 3D structures. Figure 1e shows the proposed route for synthesizing structure **1**, which contains explicit purchasable reactants with Enamine IDs. In this way, the synthesis routes of generated molecules can be greatly simplified, potentially reducing the complexity

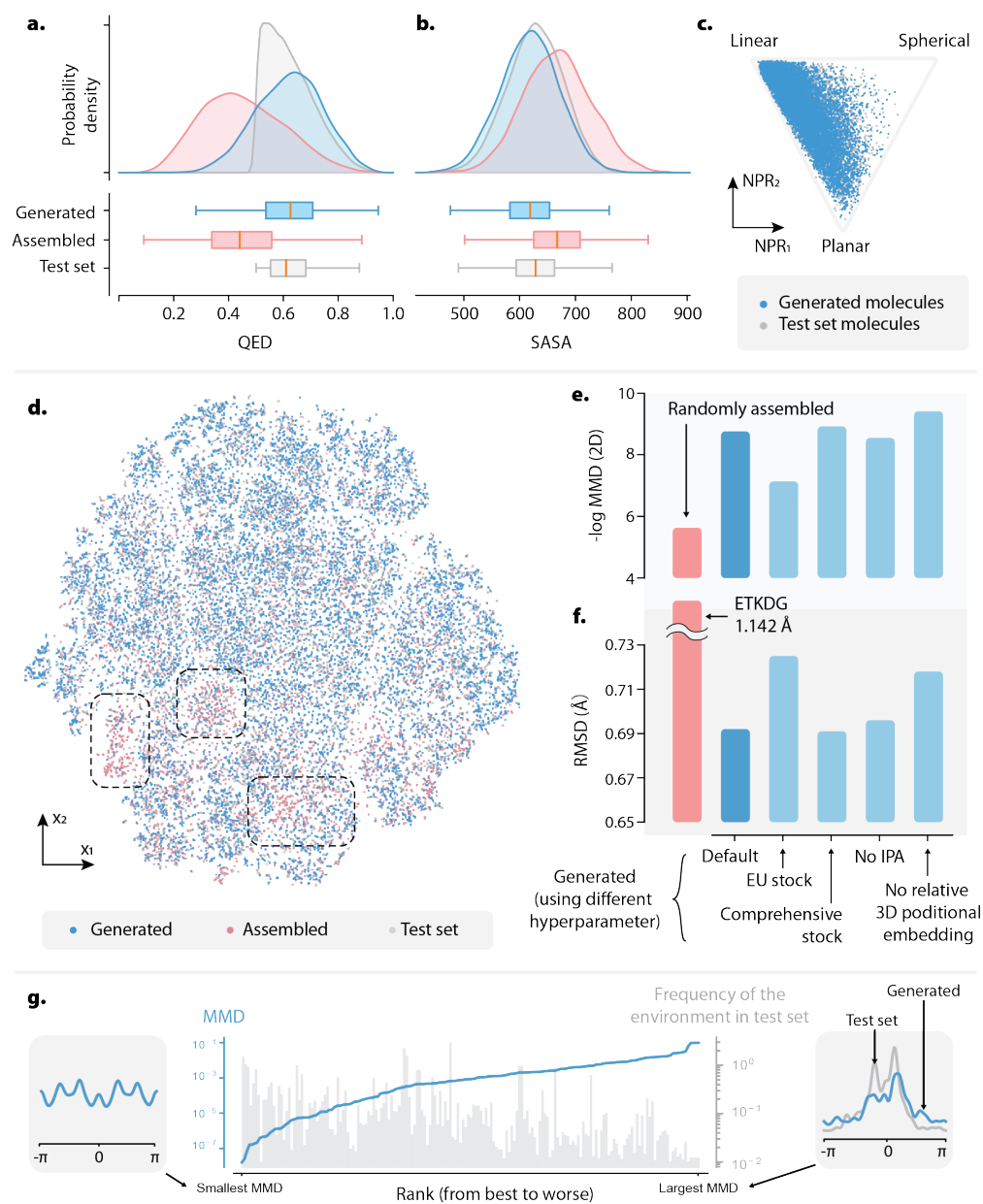


Figure 3: The performance of the unconditional generative network. **a-b.** The distribution of QED (**a.**) and SASA (**b.**) among generated (blue), randomly assembled (red), and test set (grey) molecules. **c.** The distribution of molecular shape. **d.** A visualization of the distribution of 2D Morgan fingerprints among generated (blue), randomly assembled (red), and test set (grey) molecules. Boxes with dashed borders show locations in which randomly assembled (non-druglike) molecules are enriched. **e.** The 2D MMD values (negative log scale) of generated molecules using different model configurations. The red bar shows the values calculated using randomly assembled molecules. **f.** The RMSD values of generated molecules using different model configurations. The red bar shows the RMSD values for conformers generated using ETKDG.

of wet-lab evaluations of those molecules.

### 3.1.1 Distribution of 2D and 3D molecular properties

To verify whether the model is capable of generating molecules with desirable drug-like properties, 10,000 structures are sampled from the model and several important 2D properties are calculated for each molecule. The properties include molecular weight, LogP, the number of rotatable bonds (ROT), hydrogen bond donors (HBD) and acceptors (HBA), as well as QED,<sup>49</sup> which is a widely used metric for drug-likeness estimation. The distributions of those properties are visualized in Figure S7 and Figure 3. It can be seen that the distribution of most properties matches well between the generated (blue) and test set molecules (grey). A majority of generated molecules (85%) have a QED value larger than 0.5, as shown in Figure 3a, indicating high drug-likeness.

We also compared the result with molecules randomly assembled from reactants without any drug-likeness filters (shown in red). In general, the property distribution of these randomly assembled molecules differs significantly from that of the drug-like test set, with high molecular weight and low drug-likeness. To offer a more quantitative evaluation, we calculate the sum of squared differences between the mean and the standard deviation statistics between generated and test-set molecules, as shown in Table S2. Mathematically, this metric is equivalent to the Wasserstein distance between Gaussian approximations of two distributions. The property distributions of the generated molecules are indeed more similar to the drug-like test set, compared to the randomly assembled molecules, confirming that the model can indeed significantly enrich drug-like molecules.

Similarly, several 3D molecular descriptors are calculated to examine the method’s ability to model 3D properties. Figure 3b and Figure S7g-i shows the distribution of solvent-accessible surface areas (SASA<sup>50</sup>), Polar SASA and the radius of gyration( $R_g$ <sup>51</sup>) for the generated and test set molecules. Like the 2D case, a close match between the property distributions is found. In addition, we visualized the shape distribution of these molecules

using normalized PMI ratios (NPRs<sup>52</sup>), as shown in Figure 3c. It can be seen that the generated molecules are enriched in the linear region, while tilted towards the planar region, following the distribution of test set molecules. Randomly assembled molecules show a very different distribution in most 3D properties, and quantitative measurements shown in Table S3 confirm that molecules generated by the model share higher similarity in 3D properties with the validation and test set compared with assembled ones.

### 3.1.2 The ability for the model to correctly model the drug-like chemical space

To access the network’s ability to model the drug-like space of synthesizable molecules, we visualize the distribution of 2D and 3D structures for the generated, test set, and assembled molecules, as shown in Figure 3d and Figure S8. Morgan and USRCAT<sup>53</sup> fingerprints are used to represent 2D and 3D molecule structures and t-SNE<sup>54</sup> is used for dimension reduction. The figures suggest that the overall distribution matches well between the generated (blue) and test set (grey) molecules. On the other hand, there are regions enriched with randomly assembled molecules (shown as dashed boxes in Figure 3d), which likely represent locations in chemical space featuring low drug-likeness.

To offer a more quantitative evaluation, we use maximum mean discrepancy (MMD<sup>55</sup>) to measure the overlap in the chemical space for generated and test-set molecules, as done in previous works.<sup>28,33</sup> MMD is a metric used to determine the dissimilarity between two probability distributions. Here, we also use Morgan and USRCAT fingerprints as representations for MMD calculation in 2D and 3D chemical space. Results are detailed in Table S4 and Figure 3e. We can see the MMD value is lower for molecules generated by the model compared with those randomly assembled from the building blocks, indicating higher similarity to the test set. We can conclude that after training, the network can enrich the output to the drug-like portion of the chemical space.

### 3.1.3 The quality of generated 3D structures

An important aspect of the model’s performance is its ability to generate valid 3D structures of molecules. For evaluation, we first measure its ability to correctly model the distribution of torsion angles in different environments. The environments are described using torsion SMARTS patterns by Schärfer et al.<sup>56</sup> We compare the torsion distribution between the generated and test-set molecules for each environment using MMD, and rank the value from lowest to highest, as shown in Figure 3g. Since the exact value of MMD lacks interpretability, we visually inspect the torsion distribution for the environment with the highest and lowest MMD values. Results show a good match between the distribution even for the case with the highest MMD value, indicating that the model can correctly construct the local geometries of molecules.

Next, we evaluate the global conformation quality using RMSD calculated after relaxing the generated molecules with the MMFF94s forcefield. The average RMSD values are reported in Table S4 and Figure 3f, while the distribution is shown in Figure S9. Conformations produced by the model generally have low RMSD values, with an average of 0.69Å. As a reference, the RMSD value after relaxation for conformations generated by ETKDG using the same set of topological structures is 1.14Å, a significantly higher value. ETKDG is a conformation generation method based on distance geometry and the empirical distribution of torsion angles. This method is initially developed to provide a faster alternative to MMFF94s optimization.

## 3.2 Case study: designing inhibitors targeting BTK’s ATP-binding pocket

As mentioned previously, DeepLigBuilder+ can perform pocket-based 3D molecule design by combining a pharmacophore and shape-conditioned transformer network with MCTS. To demonstrate its performance, we use DeepLigBuilder+ to design inhibitors that bind to the

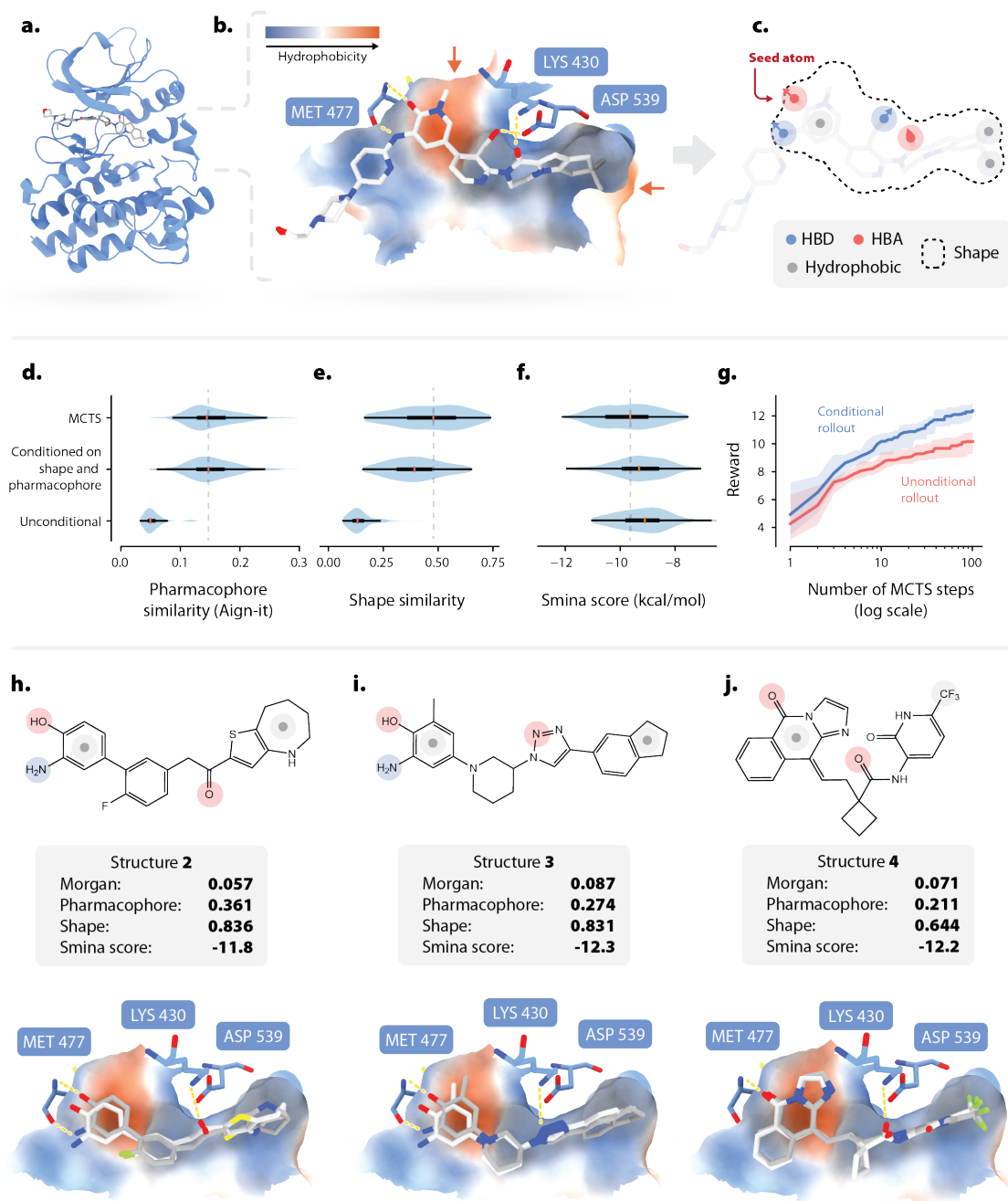


Figure 4: **a.** The structure of BTK kinase domain in complex with GDC-0853 (Fenebrutinib). **b.** The interaction between GDC-0853 and the ATP-binding pocket of BTK. **c.** The pharmacophore and shape condition extracted based on the interaction pattern. As well as the seed atom used for molecule growth. **d-f.** The distribution of: **d.** the similarity with the given pharmacophore, **e.** the similarity with the given shape, **f.** Smina docking scores inside the ATP-binding pocket of BTK, among generated molecules. **g.** The best rewards among all generated molecules at each step of MCTS. **h-j.** Several generated molecules with high predicted binding affinity. The conformation generated by the model is shown in grey, and that produced by redocking the molecule is shown in white.

ATP-binding pocket of BTK. Bruton’s tyrosine kinase (BTK) plays important roles in the signal transmission in B-cells<sup>57</sup> and is related to a series of related diseases, including B-cell malignancies<sup>58</sup> and autoimmune diseases.<sup>59</sup> Due to its importance, a variety of compounds have been developed to inhibit BTK, mostly targeting its ATP-binding pocket, with several of them approved for clinical use.<sup>60</sup> However, all currently approved inhibitors bind to BTK covalently via Cys481, which may cause off-target effects by binding with other kinases with Cys481-like residues.<sup>61</sup> Resistant mutations on Cys481 can also reduce their clinical effect.<sup>62</sup> Non-covalent binders can in theory avoid those disadvantages, and in this section, we attempt to apply DeepLigBuilder+ for the design of non-covalent BTK inhibitors.

Several non-covalent BTK inhibitors are currently under clinical investigation. Here, we extract pharmacophore features and attempt to use DeepLigBuilder+ to generate new molecules with novel structures. Figure 4a shows the structure of the kinase domain of BTK (PDB ID: 5vfi) complexed with GDC-0853 (Fenebrutinib), a potent BTK inhibitor ( $K_i=0.91\text{nM}$ ) currently under clinical trial.<sup>63</sup> GDC-0853 utilizes several important interactions inside the ATP-binding site such as hydrogen bonding with Met477, Lys430, and Asp539, as well as the hydrophobic interactions in the hinge region and the selectivity pocket (H3), as shown in Figure 4b. Based on the information, we construct the shape and pharmacophore information shown in Figure 4c, and use it as a condition for DeepLigBuilder+. Note that GDC-0853 also occupies a solvent-exposed region as seen in the left part of Figure 4b. This region is not included as input because we want to constrain the output molecule to a smaller size so that it can be more “lead-like” and easier to be further optimized. The oxygen atom of the carbonyl group is used as seed for molecule growth due to its interaction with Met477.

After the shape and pharmacophore-based inputs are determined, we combine the conditional generative model and MCTS to perform structure-based molecule design, with details shown in Section S1.6. First, we investigate whether the model can enrich molecules based on the given condition. Figure 4d-e shows that the conditional model can generate molecules

with a better match in pharmacophore and shape compared with unconditional methods. Next, we evaluate the benefit of using the conditional rollout inside MCTS. Figure 4g shows the best reward among all generated molecules at each step of MCTS. It is shown that the conditional rollout can help to speed-up MCTS search. We also evaluate the benefit of using MCTS compared with direct sampling from the conditional model. Figure 4f shows that MCTS can help to improve the docking score of generated molecules, with a 0.40 kcal/mol improvement in mean values (comparing the first row against the second row in Figure 4f). It also offers more enrichment in the range of high binding affinity. 13% of molecules generated using MCTS have a smina score  $< -10$  kcal/mol. The value is reduced to 5% if the molecules are sampled directly from the conditional network.

To better demonstrate the molecule optimization process, we visualize the search tree used in MCTS in Figure S10. Due to space constraints, the tree only contains states of the first synthon, and nodes with a visit count less than 25 are dismissed. It is shown that the model prioritizes the visits to states with higher Q-values, as those states are expanded more often. States with lower Q-values (the nodes on the left side of the tree) are less favored, due to reasons such as bad 3D positions of the synthon anchors, as shown in Figure S10.

Several generated molecules with high predicted binding affinity are shown in Figure 4h-j. A search in PubChem reveals no highly similar molecules (Tanimoto similarity  $> 95\%$ ), indicating that those are indeed novel structures. Additionally, a search in the ChEMBL database does not reveal any structurally related molecules (Tanimoto similarity  $> 70\%$ ), indicating that no topologically similar molecules have been evaluated against BTK. The topological similarity with the seed molecule extracted from GDC-0853 (Figure 4c) is also low. In contrast, in terms of pharmacophore and shape, most input pharmacophore features are covered inside these generated molecules, including hydrogen bonding with Lys430 and Met477 and hydrophobic interactions at the two ends of each molecule. Synthesis paths are also proposed by DeepLigBuilder+ for each generated molecule, making retrosynthetic analysis of generated molecules easier. For example, Figure 6a shows the proposed synthetic



path for Structure **4**. The path for Structure **2** and **3** are shown in Figure S12. In summary, by combining MCTS with the conditional generative model, DeepLigBuilder+ can enrich molecules with high binding affinity based on the pharmacophore constraint.

### 3.3 Case study: designing inhibitors targeting the NAD<sup>+</sup> pocket of PHGDH

Targeting cancer metabolism represents an important strategy for cancer drug development.<sup>64</sup> Human phosphoglycerate dehydrogenase (PHGDH), a key enzyme in the serine biosynthesis pathway, has been demonstrated to have crucial roles in tumorigenesis,<sup>65</sup> making it a promising cancer-related target. One strategy for targeting PHGDH is to design inhibitors that bind to its NAD<sup>+</sup> pocket. Multiple such inhibitors have been reported in previous works, with most of them containing an indole-based scaffold. In this case study, we use DeepLigBuilder+ to design potential binders for the NAD<sup>+</sup> pocket with novel structures.

Figure 5a shows the structure of PHGDH (PDB ID: 6plg) together with compound **15**, a potent inhibitor of the target developed by Mullarky et al.<sup>66</sup> Figure 5b demonstrates the interaction between the ligand and the target. The nitrogen atom in the amide group in compound **15** acts as a hydrogen bond donor and interacts with Asp175. The carboxyl group in compound **15** can form hydrogen bonds with backbone nitrogen atoms. It also forms charge-charge interaction with Arg155. The indole structure of compound **15** resides inside a hydrophobic region, as shown by the orange arrow in Figure 5b. A pharmacophore model is constructed based on those interactions, as shown in Figure 5c. We use the amide structure as the seed for molecule growth, as shown in Figure 5c and Figure S13b. The shape of compound **15** is also used as an input feature.

Next, we use DeepLigBuilder+ to generate molecules based on the pharmacophore and shape information and the target structure. Similar to the previous section, we first evaluate whether the conditional model offers more enriched results based on the provided information. Indeed, Figure 5d-e shows that molecules sampled from the conditional transformer

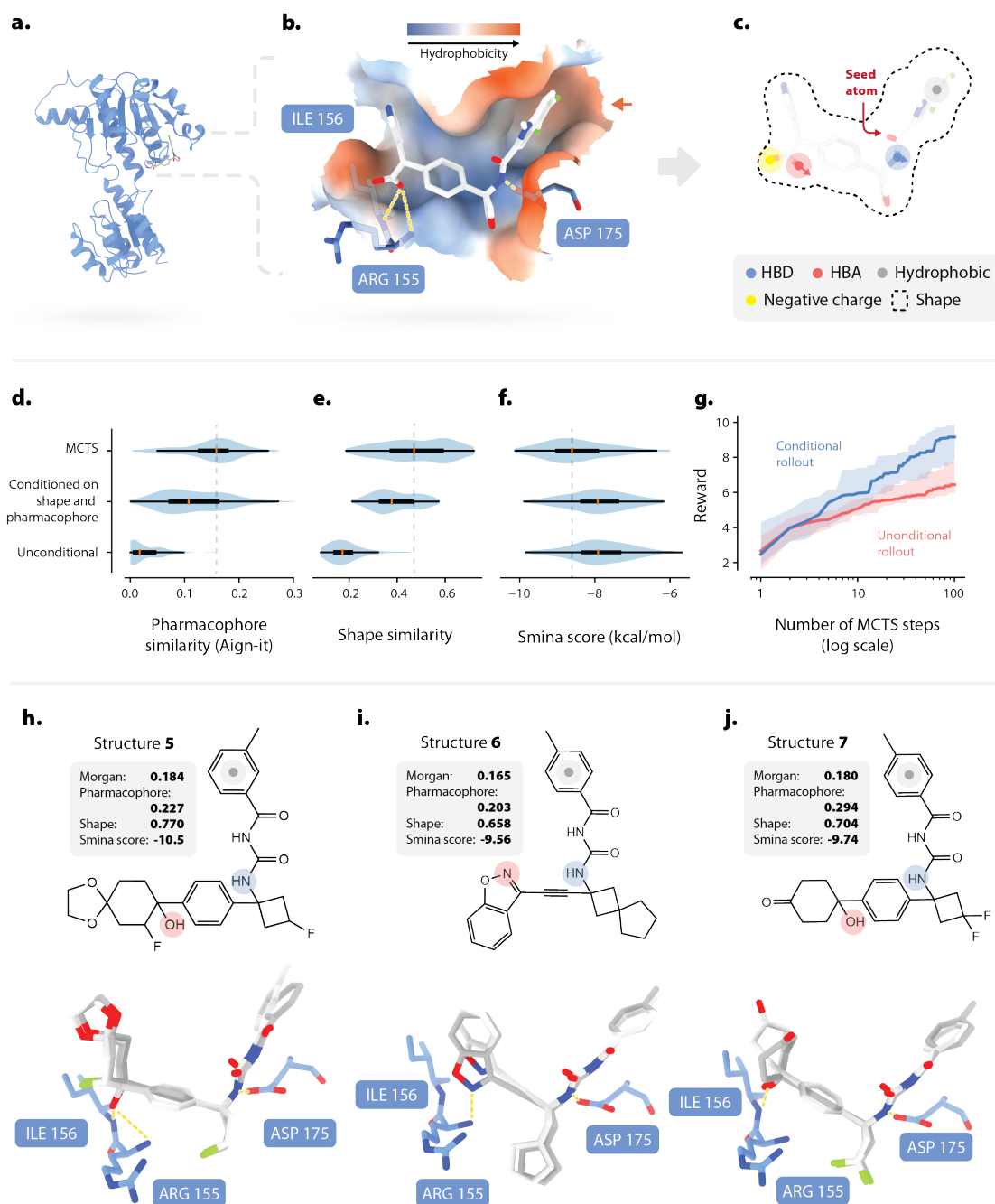


Figure 5: **a.** The structure of PHGDH with compound 15. **b.** The interaction between compound 15 with the NAD<sup>+</sup> binding pocket of PHGDH. **c.** The pharmacophore and shape condition extracted based on the interaction pattern. As well as the seed atom used for molecule growth. **d-f.** The distribution of: **d.** the similarity with the given pharmacophore, **e.** the similarity with the given shape, **f.** Smina docking scores inside the NAD<sup>+</sup> binding pocket of PHGDH, among generated molecules. **g.** The best rewards among all generated molecules at each step of MCTS. **h-j.** Several generated molecules with high predicted binding affinity. The conformation generated by the model is shown in grey, and that produced by redocking the molecule is shown in white.

match better to the input pharmacophore(Figure 5d) and shape(Figure 5e) compared with the unconditional model. Figure 5g shows that introduction conditions help to accelerate the MCTS search, as demonstrated by the blue curve. When evaluating the benefit of the MCTS module, we found that MCTS search helps the model to generate molecules with better pharmacophore and shape matches (Figure 5d-e), and also helps to improve the docking score of the result, with an average improvement of Smina score of 0.53 kcal/mol. 11% of molecules generated using MCTS have a Smina score  $< -9.5$  kcal/mol, compared to the value of 2% for those directly sampled from the conditional model.

Figure 5h-j shows several molecules generated by DeepLigBuilder+ with high predicted binding affinity. The reaction paths generated by the model are shown in Figure 6b and Figure S14. Those molecules have low topological similarities with compound **15**, but share pharmacophore features such as hydrogen bond donors that interact with Asp175 and acceptors that interact with Ile156 or Arg155. A search in PubChem does not reveal results with high topological similarity with those molecules (Tanimoto similarity  $>95\%$ ), indicating that those are indeed novel structures. Also, the ChEMBL dataset does not contain topologically related compound records (Tanimoto similarity  $>70\%$ ), which means that similar molecules are not yet evaluated against PHGDH. Interestingly, those molecules contain cyclobutane structures that are similar to the oxetane structure in compound **15**. This structural motif helps to form a turn in the molecule shape for better accommodation with the pocket, and also creates a hydrophobic interaction with Ile177.

### 3.4 Ablation studies and the effects of different hyperparameters

It is important to understand how different architectural and hyperparameter choices affect the performance of the proposed model. In this section, we demonstrate the impact of several important network features and hyperparameters. Details about the configurations explored are shown in Table S1. The performances of the model under different configurations are shown in Table S4.

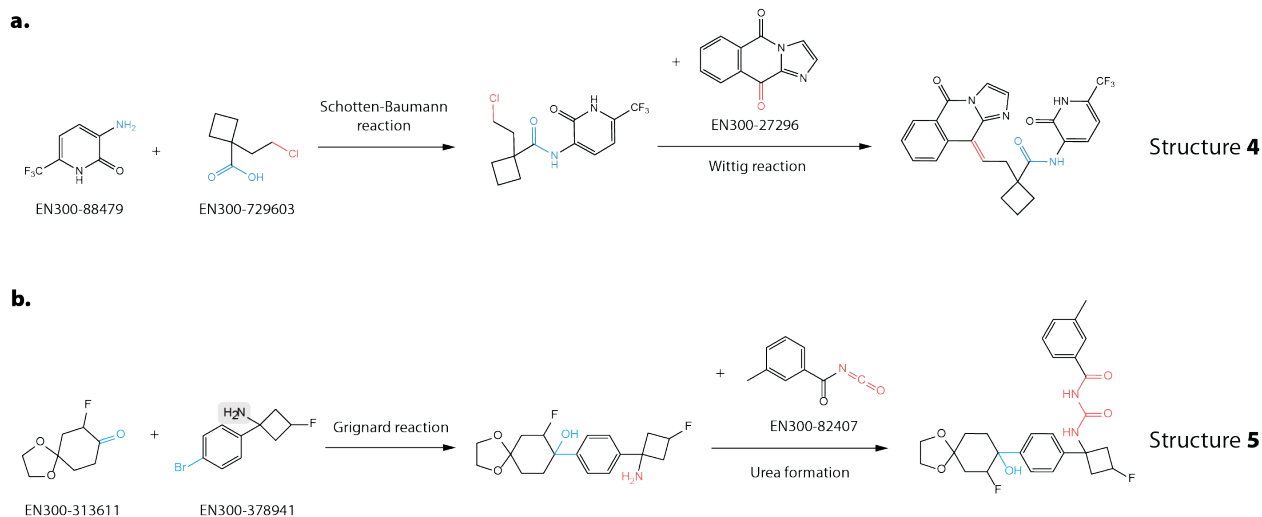


Figure 6: **a.** The synthetic path of Structure 4 proposed by DeepLigBuilder+. It involves a two-step process, which first connects the amide bond using the Schotten-Baumann reaction, and then forms the double bond using the Wittig reaction. Enamine IDs of reactants are also given. Note that the Schotten-Baumann reaction requires an additional activation step that transforms the carboxyl group into the acyl chloride. Also, the Wittig reaction requires the formation of the ylide. **b.** The synthetic path of Structure 5 proposed by DeepLigBuilder+. The first two reactants are connected using the Grignard reaction. The third reactant is connected by forming a urea structure using the amine group and the isocyanate group. Note that before the first step, reactant 2 needs to be transformed into the Grignard reagent. Additionally, the amine group in reactant 2 (marked grey) needs to be protected before carrying out other reactions.

### 3.4.1 The effect of changing the set of accessible building blocks

A major feature of DeepLigBuilder+ is its capability to suggest synthetic paths with accessible building blocks along with its generated molecules. However, the accessibility of building blocks is a constantly changing factor. On one hand, due to technical advances, the number of synthesizable building blocks is rapidly growing over the years. On the other hand, in-stock supply of such building blocks may vary between times and locations, and most require on-demand synthesis, increasing the cost. Ideally, DeepLigBuilder+ should allow the user to choose a building block set that fits their need, without the need to perform re-training. Here, we simulate such scenarios and report how the choice of building blocks impacts the quality of generated molecules.

To simulate the lack of in-stock availability for certain building blocks, we restrict the building blocks to the EU stock, which is a smaller set with 81,235 compounds. In terms of the quality of topological structures, although Figure 3e shows that there is an increase in the MMD value after the restriction, Table S2 confirms that the generated molecules still maintain a high drug-likeness, with an average QED value of 0.60, close to the value before changing the building blocks. In terms of the quality of 3D conformation, Table S4 and Figure 3f indicates an increase of RMSD from 0.69Å to 0.72Å, but still much lower than 1Å. From the results, we believe that although using a smaller building block may indeed impact the performance of the network, such an effect should be minor and still allows for regular application of DeepLigBuilder+ in drug design tasks.

Then, to demonstrate how increasing the building block set may affect the generation result, we expand to include the comprehensive catalog, which contains more than 1 million (1,162,033) compounds, some may be synthesized on-demand. Figure 3e-f shows that this change induces little impact on the performance of the output. Only 28.1% of molecules generated have used the newly added building blocks. In conclusion, we believe that DeepLigBuilder+ still offers promising performance when the building block set is changed, but a re-training may be required if we want to fully utilize newly added building blocks.

### 3.4.2 The effect of different ways to encode 3D structural information

Besides using the relative 3D positional encoding module to incorporate 3D information, DeepLigBuilder+ also uses invariant point attention (IPA), which offers a geometrically-aware way to pass information between atoms. To understand the benefit of including IPA, we disable the two modules consecutively and investigate the impact of those changes. The results are shown in Figure 3e-f and Table S4. We found that removing IPA has little impact on the quality of 3D conformation, as measured by RMSD, showing that IPA is not essential for maintaining 3D structure quality. However, the quality of 2D structure, as measured by 2D MMD, is reduced. If we remove the 3D positional embedding and keep IPA, we observe a significant improvement in 2D structural quality, but the RMSD value increased to 0.718Å.

The results above demonstrated a trade-off between 2D and 3D structural quality, and that the two ways of including 3D information, IPA and relative positional encoding, have different emphases on the two aspects. One way to understand the result is to view IPA as a more regularized way of encoding geometric information. Our previous work has demonstrated that the model can not reliably generate correct 2D structures if it overly relies on accurate 3D information since it reduces the model’s ability to recover from errors during generation.<sup>33</sup> The highly structured way to communicate 3D information in IPA can act as a form of regularization on how the model uses the 3D information. On the other hand, there is no limitation on how 3D relative positional embedding will be processed by the network. Therefore, although the model can still generate accurate 3D structures without IPA, a lack of regularization will reduce the quality of 2D structures. Using both modules acts as a compromise, with an improved 3D conformation quality and a balanced 2D structure quality.

## 4 Conclusion

We have developed a new de novo drug design tool, DeepLigBuilder+, that generates synthesis-driven 3D molecules for a given target. DeepLigBuilder+ uses geometric transformer combined with an MCTS-based reinforcement learning module to navigate the space of synthesizable 3D molecules to identify potential bioactive compounds. This method aims to address two major challenges faced by deep molecule generative models: (1) the design of 3D molecules based on 3D constraints, and (2) the design of molecules with high synthetic accessibility. DeepLigBuilder+ has shown promising performances in overcoming these challenges. DeepLigBuilder+ is capable of generating 3D molecules with high drug-likeness and geometric quality under the synthetic accessibility constraint. In the case study related to BTK and PHGDH, DeepLigBuilder+ significantly enriches molecules with high docking scores and favorable interaction patterns with the target pocket, using the 3D information provided. For each generated molecule, DeepLigBuilder+ proposes a synthetic route with explicit reactions and building blocks that can be directly queried from the supplier, making retrosynthetic analysis much easier.

DeepLigBuilder+ takes advantage of recent developments in 3D generative networks<sup>33</sup> and the idea of synthetically aware de novo design.<sup>37</sup> To restrict the model to the chemical space of synthesizable molecules, we develop a method that calculates a stepwise constraint of the generation trajectory to ensure that it leads to purchasable building blocks. Compared to other approaches that require a fragment-based generation scheme, our method can in theory be applied to various atom-based molecule generative models. In addition, it offers better scalability to large building block datasets by organizing them into a tree-based structure and avoids full database scans at each step. To achieve structure-based generation, we constructed a new dataset of pharmacophore-ligand pairs using large-scale 3D alignment of molecules, and then use it to develop a novel SE(3)-equivariant transformer conditioned on 3D information. This network is then combined with MCTS as the rollout policy, and it is demonstrated that the combination results in a significant improvement in the search speed

of MCTS.

DeepLigBuilder+ could be improved in the following aspects in the future. First, the present molecule assembling process relies on simple SMARTS rules, which may be limited in precision. We are planning to include a more dedicated model for yield and selectivity prediction so that we can further improve the synthesizability of the assembled molecules by the model. Second, we are planning to update the reaction set to include broader, more modern reactions. In addition, the current version of DeepLigBuilder+ requires user-provided seed structures for molecule growth, and we are planning to develop methods to automate the seed selection process. Finally, we are planning to build a transformer model that is directly conditioned on the 3D pocket structure, without the need for pharmacophore extraction. In summary, due to its unique capability of generating highly synthesizable molecules with 3D structures, DeepLigBuilder+ provides a powerful tool to generate bioactive molecules and to accelerate the process of structure-based drug design.

## 5 Acknowledgements

This work has been supported in part by the National Natural Science Foundation of China (22033001). We would like to thank Yuhao Ren and Kangjie Lin for their kind advice on the synthetic accessibility of generated molecules. We also appreciate Alibaba Cloud for providing the EFLOPS computation platform for the GPU-based network training.

## References

- (1) Paul, S. M.; Mytelka, D. S.; Dunwiddie, C. T.; Persinger, C. C.; Munos, B. H.; Lindborg, S. R.; Schacht, A. L. How to improve R&D productivity: the pharmaceutical industry’s grand challenge. *Nature Reviews Drug Discovery* **2010**, *9*, 203–214.
- (2) Trott, O.; Olson, A. J. AutoDock Vina: Improving the speed and accuracy of docking



- with a new scoring function, efficient optimization, and multithreading. *Journal of Computational Chemistry* **2010**, *31*, 455–461.
- (3) Lyu, J.; Wang, S.; Balias, T. E.; Singh, I.; Levit, A.; Moroz, Y. S.; O’Meara, M. J.; Che, T.; Alga, E.; Tolmacheva, K.; Tolmachev, A. A.; Shoichet, B. K.; Roth, B. L.; Irwin, J. J. Ultra-large library docking for discovering new chemotypes. *Nature* **2019**, *566*, 224–229.
- (4) Gorgulla, C.; Boeszoermenyi, A.; Wang, Z.-F.; Fischer, P. D.; Coote, P. W.; Das, K. M. P.; Malets, Y. S.; Radchenko, D. S.; Moroz, Y. S.; Scott, D. A.; Fackeldey, K.; Hoffmann, M.; Iavniuk, I.; Wagner, G.; Arthanari, H. An open-source drug discovery platform enables ultra-large virtual screens. *Nature* **2020**, *580*, 663–668.
- (5) Schneider, G.; Fechner, U. Computer-based de novo design of drug-like molecules. *Nature Reviews Drug Discovery* **2005**, *4*, 649–663.
- (6) Nishibata, Y.; Itai, A. Automatic creation of drug candidate structures based on receptor structure. Starting point for artificial lead generation. *Tetrahedron* **1991**, *47*, 8985–8990.
- (7) Böhm, H.-J. The computer program LUDI: A new method for the de novo design of enzyme inhibitors. *Journal of Computer-Aided Molecular Design* **1992**, *6*, 61–78.
- (8) Pearlman, D. A.; Murcko, M. A. CONCEPTS: New dynamic algorithm for de novo drug suggestion. *Journal of Computational Chemistry* **1993**, *14*, 1184–1193.
- (9) Wang, R.; Gao, Y.; Lai, L. LigBuilder: A Multi-Purpose Program for Structure-Based Drug Design. *Molecular modeling annual* **2000**, *6*, 498–516.
- (10) Yuan, Y.; Pei, J.; Lai, L. LigBuilder 2: A Practical de Novo Drug Design Approach. *Journal of Chemical Information and Modeling* **2011**, *51*, 1083–1091.

- (11) Yuan, Y.; Pei, J.; Lai, L. LigBuilder V3: A Multi-Target de novo Drug Design Approach. *Frontiers in Chemistry* **2020**, *8*, 142.
- (12) Schneider, G. Designing the molecular future. *Journal of Computer-Aided Molecular Design* **2012**, *26*, 115–120.
- (13) Schneider, G.; Clark, D. E. Automated De Novo Drug Design: Are We Nearly There Yet? *Angewandte Chemie International Edition* **2019**, *58*, 10792–10803.
- (14) Ni, S.; Yuan, Y.; Huang, J.; Mao, X.; Lv, M.; Zhu, J.; Shen, X.; Pei, J.; Lai, L.; Jiang, H.; Li, J. Discovering Potent Small Molecule Inhibitors of Cyclophilin A Using de Novo Drug Design Approach. *Journal of Medicinal Chemistry* **2009**, *52*, 5295–5298.
- (15) Shang, E.; Yuan, Y.; Chen, X.; Liu, Y.; Pei, J.; Lai, L. De Novo Design of Multitarget Ligands with an Iterative Fragment-Growing Strategy. *Journal of Chemical Information and Modeling* **2014**, *54*, 1235–1241.
- (16) Park, H.; Hong, S.; Kim, J.; Hong, S. Discovery of Picomolar ABL Kinase Inhibitors Equipotent for Wild Type and T315I Mutant via Structure-Based de Novo Design. *Journal of the American Chemical Society* **2013**, *135*, 8227–8237.
- (17) Xu, Y.; Lin, K.; Wang, S.; Wang, L.; Cai, C.; Song, C.; Lai, L.; Pei, J. Deep learning for molecular generation. *Future Medicinal Chemistry* **2019**, *11*, 567–597.
- (18) Segler, M. H. S.; Kogej, T.; Tyrchan, C.; Waller, M. P. Generating Focused Molecule Libraries for Drug Discovery with Recurrent Neural Networks. *ACS Central Science* **2017**, *4*, 120–131.
- (19) Li, Y.; Zhang, L.; Liu, Z. Multi-objective de novo drug design with conditional graph generative model. *Journal of Cheminformatics* **2018**, *10*, 33.
- (20) Jin, W.; Barzilay, R.; Jaakkola, T. Junction Tree Variational Autoencoder for Molecular Graph Generation. *arXiv* **2018**, <https://arxiv.org/abs/1802.04364>.

- (21) You, J.; Ying, R.; Ren, X.; Hamilton, W. L.; Leskovec, J. GraphRNN: Generating Realistic Graphs with Deep Auto-regressive Models. *arXiv* **2018**,
- (22) Gómez-Bombarelli, R.; Wei, J. N.; Duvenaud, D.; Hernández-Lobato, J. M.; Sánchez-Lengeling, B.; Sheberla, D.; Aguilera-Iparraguirre, J.; Hirzel, T. D.; Adams, R. P.; Aspuru-Guzik, A. Automatic Chemical Design Using a Data-Driven Continuous Representation of Molecules. *ACS Central Science* **2018**, *4*, 268–276.
- (23) Guimaraes, G. L.; Sanchez-Lengeling, B.; Outeiral, C.; Farias, P. L. C.; Aspuru-Guzik, A. Objective-Reinforced Generative Adversarial Networks (ORGAN) for Sequence Generation Models. *arXiv* **2017**, <https://arxiv.org/abs/1705.10843>.
- (24) Cao, N. D.; Kipf, T. MolGAN: An implicit generative model for small molecular graphs. *arXiv* **2018**, <https://arxiv.org/abs/1805.11973>.
- (25) Olivecrona, M.; Blaschke, T.; Engkvist, O.; Chen, H. Molecular de-novo design through deep reinforcement learning. *Journal of Cheminformatics* **2017**, *9*, 48.
- (26) You, J.; Liu, B.; Ying, R.; Pande, V.; Leskovec, J. Graph Convolutional Policy Network for Goal-Directed Molecular Graph Generation. *arXiv* **2018**, <https://arxiv.org/abs/1806.02473>.
- (27) Imrie, F.; Bradley, A. R.; Schaar, M. v. d.; Deane, C. M. Deep Generative Models for 3D Linker Design. *Journal of Chemical Information and Modeling* **2020**, *60*, 1983–1995.
- (28) Li, Y.; Hu, J.; Wang, Y.; Zhou, J.; Zhang, L.; Liu, Z. DeepScaffold: A Comprehensive Tool for Scaffold-Based De Novo Drug Discovery Using Deep Learning. *Journal of Chemical Information and Modeling* **2019**, *60*, 77–91.
- (29) Zhavoronkov, A. et al. Deep learning enables rapid identification of potent DDR1 kinase inhibitors. *Nature Biotechnology* **2019**, *37*, 1038–1040.

- (30) Skalic, M.; Sabbadin, D.; Sattarov, B.; Sciabola, S.; Fabritiis, G. D. From Target to Drug: Generative Modeling for the Multimodal Structure-Based Ligand Design. *Molecular Pharmaceutics* **2019**, *16*, 4282–4291.
- (31) Xu, M.; Ran, T.; Chen, H. De Novo Molecule Design Through the Molecular Generative Model Conditioned by 3D Information of Protein Binding Sites. *Journal of Chemical Information and Modeling* **2021**, *61*, 3240–3254.
- (32) Masuda, T.; Ragoza, M.; Koes, D. R. Generating 3D Molecular Structures Conditional on a Receptor Binding Site with Deep Generative Models. *arXiv* **2020**, <https://arxiv.org/abs/2010.14442>.
- (33) Li, Y.; Pei, J.; Lai, L. Structure-based de novo drug design using 3D deep generative models. *Chemical Science* **2021**, *12*, 13664–13675.
- (34) Peng, X.; Luo, S.; Guan, J.; Xie, Q.; Peng, J.; Ma, J. Pocket2Mol: Efficient Molecular Sampling Based on 3D Protein Pockets. *arXiv* **2022**,
- (35) Igashov, I.; Stärk, H.; Vignac, C.; Satorras, V. G.; Frossard, P.; Welling, M.; Bronstein, M.; Correia, B. Equivariant 3D-Conditional Diffusion Models for Molecular Linker Design. *arXiv* **2022**,
- (36) Gao, W.; Coley, C. W. The Synthesizability of Molecules Proposed by Generative Models. *Journal of Chemical Information and Modeling* **2020**, *60*, 5714–5723.
- (37) Coley, C. W. Defining and Exploring Chemical Spaces. *Trends in Chemistry* **2020**, *3*, 133–145.
- (38) Vinkers, H. M.; Jonge, M. R. d.; Daeyaert, F. F. D.; Heeres, J.; Koymans, L. M. H.; Lenthe, J. H. v.; Lewi, P. J.; Timmerman, H.; Aken, K. V.; Janssen, P. A. J. SYNOPSIS: SYNthesize and OPTimize System in Silico. *Journal of Medicinal Chemistry* **2003**, *46*, 2765–2773.

- (39) Hartenfeller, M.; Zettl, H.; Walter, M.; Rupp, M.; Reisen, F.; Proschak, E.; Weggen, S.; Stark, H.; Schneider, G. DOGS: Reaction-Driven de novo Design of Bioactive Compounds. *PLoS Computational Biology* **2012**, *8*, e1002380.
- (40) Bradshaw, J.; Paige, B.; Kusner, M. J.; Segler, M. H. S.; Hernández-Lobato, J. M. A Model to Search for Synthesizable Molecules. *arXiv* **2019**,
- (41) Bradshaw, J.; Paige, B.; Kusner, M. J.; Segler, M. H.; Hernandez-Lobato, J. M. Barking up the right tree: an approach to search over molecule synthesis DAGs. *arXiv preprint arXiv:2012.11522* **2020**,
- (42) Gottipati, S. K.; Sattarov, B.; Niu, S.; Pathak, Y.; Wei, H.; Liu, S.; Thomas, K. M. J.; Blackburn, S.; Coley, C. W.; Tang, J.; Chandar, S.; Bengio, Y. Learning To Navigate The Synthetically Accessible Chemical Space Using Reinforcement Learning. *arXiv* **2020**,
- (43) Gao, W.; Mercado, R.; Coley, C. W. Amortized Tree Generation for Bottom-up Synthesis Planning and Synthesizable Molecular Design. *arXiv* **2021**,
- (44) Hartenfeller, M.; Eberle, M.; Meier, P.; Nieto-Oberhuber, C.; Altmann, K.-H.; Schneider, G.; Jacoby, E.; Renner, S. A Collection of Robust Organic Synthesis Reactions for In Silico Molecule Design. *Journal of Chemical Information and Modeling* **2011**, *51*, 3093–3098.
- (45) Jumper, J. et al. Highly accurate protein structure prediction with AlphaFold. *Nature* **2021**, *596*, 583–589.
- (46) Xiao, C.; Huang, R.; Mei, J.; Schuurmans, D.; Muller, M. Maximum entropy monte-carlo planning. *Advances in Neural Information Processing Systems* **2019**, *32*, 9520–9528.

- (47) Koes, D. R.; Baumgartner, M. P.; Camacho, C. J. Lessons Learned in Empirical Scoring with smina from the CSAR 2011 Benchmarking Exercise. *Journal of Chemical Information and Modeling* **2013**, *53*, 1893–1904.
- (48) Giordano, D.; Biancaniello, C.; Argenio, M. A.; Facchiano, A. Drug Design by Pharmacophore and Virtual Screening Approach. *Pharmaceuticals* **2022**, *15*, 646.
- (49) Bickerton, G. R.; Paolini, G. V.; Besnard, J.; Muresan, S.; Hopkins, A. L. Quantifying the chemical beauty of drugs. *Nature Chemistry* **2012**, *4*, 90–98.
- (50) Mitternacht, S. FreeSASA: An open source C library for solvent accessible surface area calculations. *F1000Research* **2016**, *5*, 189.
- (51) Todeschini, R.; Consonni, V. Descriptors from Molecular Geometry. **2003**, 1004–1033.
- (52) Sauer, W. H. B.; Schwarz, M. K. Molecular Shape Diversity of Combinatorial Libraries: A Prerequisite for Broad Bioactivity †. *Journal of Chemical Information and Computer Sciences* **2003**, *43*, 987–1003.
- (53) Schreyer, A. M.; Blundell, T. USRCAT: real-time ultrafast shape recognition with pharmacophoric constraints. *Journal of Cheminformatics* **2012**, *4*, 27.
- (54) Maaten, L. V. d.; Hinton, G. Visualizing Data using t-SNE. *Journal of machine learning research* **2008**, *9*, 2579-2605.
- (55) Gretton, A.; Borgwardt, K. M.; Rasch, M. J.; Scholkopf, B.; Smola, A. A kernel two-sample test. *The Journal of Machine Learning Research* **2012**, *13*, 723–773.
- (56) Schärfer, C.; Schulz-Gasch, T.; Ehrlich, H.-C.; Guba, W.; Rarey, M.; Stahl, M. Torsion Angle Preferences in Druglike Chemical Space: A Comprehensive Guide. *Journal of Medicinal Chemistry* **2013**, *56*, 2016–2028.
- (57) Satterthwaite, A. B.; Li, Z.; Witte, O. N. Btk function in B cell development and response. *Seminars in Immunology* **1998**, *10*, 309–316.

- (58) Singh, S. P.; Dammeijer, F.; Hendriks, R. W. Role of Bruton's tyrosine kinase in B cells and malignancies. *Molecular Cancer* **2018**, *17*, 57.
- (59) Zhang, D.; Gong, H.; Meng, F. Recent Advances in BTK Inhibitors for the Treatment of Inflammatory and Autoimmune Diseases. *Molecules* **2021**, *26*, 4907.
- (60) Tasso, B.; Spallarossa, A.; Russo, E.; Brullo, C. The Development of BTK Inhibitors: A Five-Year Update. *Molecules* **2021**, *26*, 7411.
- (61) Sibaud, V.; Beylot-Barry, M.; Protin, C.; Vigarios, E.; Recher, C.; Ysebaert, L. Dermatological Toxicities of Bruton's Tyrosine Kinase Inhibitors. *American Journal of Clinical Dermatology* **2020**, *21*, 799–812.
- (62) Woyach, J. A. et al. Resistance Mechanisms for the Bruton's Tyrosine Kinase Inhibitor Ibrutinib. *The New England Journal of Medicine* **2014**, *370*, 2286–2294.
- (63) Crawford, J. J. et al. Discovery of GDC-0853: A Potent, Selective, and Noncovalent Bruton's Tyrosine Kinase Inhibitor in Early Clinical Development. *Journal of Medicinal Chemistry* **2018**, *61*, 2227–2245.
- (64) Faubert, B.; Solmonson, A.; DeBerardinis, R. J. Metabolic reprogramming and cancer progression. *Science* **2020**, *368*.
- (65) Zhao, J.-Y.; Feng, K.-R.; Wang, F.; Zhang, J.-W.; Cheng, J. F.; Lin, G.-Q.; Gao, D.; Tian, P. A Retrospective Overview of PHGDH and Its Inhibitors for Regulating Cancer Metabolism. *European Journal of Medicinal Chemistry* **2021**, *217*, 113379.
- (66) Mullarky, E. et al. Inhibition of 3-Phosphoglycerate Dehydrogenase (PHGDH) by Indole Amides Abrogates de novo Serine Synthesis in Cancer Cells. *Bioorganic & Medicinal Chemistry Letters* **2019**, *29*, 2503–2510.

# Supporting Information:

## Synthesis-driven design of 3D molecules for structure-based drug discovery using geometric transformers

Yibo Li,<sup>†</sup> Jianfeng Pei,<sup>\*,‡</sup> and Luhua Lai<sup>\*,†,‡,¶</sup>

<sup>†</sup> *Center for Life Sciences, Academy for Advanced Interdisciplinary Studies, Peking University, Beijing 100871, China*

<sup>‡</sup> *Center for Quantitative Biology, Academy for Advanced Interdisciplinary Studies, Peking University, Beijing 100871, China*

<sup>¶</sup> *BNLMS, College of Chemistry and Molecular Engineering, Peking University, Beijing 100871, China*

E-mail: jfpei@pku.edu.cn; lhlai@pku.edu.cn

## 1 Supplementary Methods

### 1.1 Constructing the synthon dataset

We use the building block sets provided by Enamine as the set of purchasable reactants. The global stock, which contains 238,980 compounds at the time of access (July 2022), is used to assemble the training set molecules. To investigate the impact of changing available reactants on the model’s performance, we also downloaded the EU stock and comprehensive catalog, which contains 81,235 and 1,162,033 molecules respectively (by Oct 2022).



For reactions, we use the 58 SMARTS rules collected by Hartenfeller et al.,<sup>S1</sup> which represents a set of robust chemical reactions relevant to drug design. Based on the reaction set, we constructed a set of SMARTS rules to convert reactants to synthons. The conversion is performed using the following procedure:

- (1) For a given building block and reaction rule, we predict the product structure using RDKit. If the reaction involves two reactants, the other reactant is set to be a minimum structure with the required function group.
- (2) The substructure in the product molecule that corresponds to the building block is extracted. The open valences resulting from the bond break in the extracted substructure are labeled with the reaction type and its role in the reaction.
- (3) If the substructure extraction results in multiple valences, this indicates that new rings are formed after the reaction. In this case, we either include the new ring structure inside this synthon or leave the ring to the synthon corresponding to the other reactant.

A visual demonstration of this process is given in Figure S1 and Figure S2. To simplify the generative model, we require that each reaction will result in at most one open valence in synthon structures, and such valence must correspond to a single bond in the product molecule. Most reactions satisfy this requirement. As a result, we kept 52 reactions and constructed 108 SMARTS rules for converting reactants to synthons.

The Enamine building blocks are then converted to synthons using those rules. For each building block, we enumerate all possible synthon structures by iterating through the reaction rules. At most two reactions are allowed to happen in one reactant. To ensure that the generated synthons are fragment-like and relevant to drug discovery, we apply the following rules to filter the results:

- (1) Element types of atoms inside each molecule are restricted to the set {C, O, N, P, S, F, Cl, Br, I} and bond types are restricted to single, double, triple, and aromatic bonds.

- (2) Synthons are required to be “fragment-like” based on the rule of two (Ro2).<sup>S2</sup>
- (3) Each fragment can have at most 4 rings, and the size of each ring should not be larger than 7.
- (4) Since we are focusing on designing non-covalent binders, we filter structures with the potential of forming covalent bonds with the protein, using a set of SMARTS rules.<sup>S3</sup>

The filtering results in a dataset containing 241,310 synthons from the global stock, 103,385 synthons from the EU stock, and 783,195 synthons from the comprehensive catalog. The synthons from the global stock are later used to assemble the training set molecules (See Section S1.5).

## 1.2 Performing molecule generation

DeepLigBuilder+ generates 3D molecules using a synthon-based method. Each molecule is composed of 3 synthon structures, which is equivalent to combining three building blocks with two reaction steps. When generating each synthon, DeepLigBuilder+ uses a graph-based approach similar to our previous work.<sup>S4</sup> Specifically, the model generates 3D synthon structures by producing molecular graphs. We write the output graph as  $G = (V, E, A, B, X)$ , where  $V$  and  $E$  are the set of nodes (atoms) and edges (bonds),  $A = \{a_v\}_{v \in V}$  and  $B = \{b_{uv}\}_{\{u,v\} \in E}$  are labels representing the type of each atom and bond, and  $X = \{\mathbf{x}_v\}_{v \in V}$  are the 3D coordinates of each atom.

When generating each synthon, the model starts with an empty graph  $G_0 = (, \dots, )$ , iteratively updates its structure  $G_t = a_t(G_{t-1})$ , and outputs the graph as a new synthon fragment when it is ready. During generating, additional information is attached to each node in the graph to record the generation history, which includes:

- (1) The currently focused node, denoted as  $v_t^*$ , where  $t$  represents the step ID. The definition of a “focused” node is similar to that in our previous works.<sup>S4</sup> Briefly, all edits to

the molecular graph, whether to add new atoms or new bonds, happen on the focused node.

- (2) The parent of each node  $P_t = \{p_v\}_{v \in V_t}$ . A node  $p_v$  is called the “parent” of another node  $v$  if  $p_v$  is the focused node when  $v$  is generated. Note that the parent-child relationship induces a spanning tree of the molecular graph  $G_t$ , which can be used to calculate tree-based distances between atoms (or nodes) in the graph as input features to the transformer network (as detailed in Section S1.4).

We denote the state of the molecular graph at step  $t$  with the additional information as  $G'_t = (V_t, E_t, A_t, B_t, X_t, v_t^*, P_t)$ . The graph structure is iteratively modified based on actions  $a_t$  sampled from the neural network. The following types of actions are allowed during generation:

- (1) Initialization, which adds the first atom to the molecular graph;
- (2) Append, which attaches a new atom to the focused atom using a new bond. For this action, the model needs to decide the type of the new atom and bond, as well as the 3D position of the new atom. When generating the position, the model uses a spherical coordinate frame attached to the focused atom, following our previous work.<sup>S4</sup> Besides the element type of the new atom, the model also needs to decide whether there will be branches on this atom and whether the atom will be a target of future ring closure, similar to Ahn et al.<sup>S5</sup>
- (3) Backtracking, which requires the model to move the focused atom to its closest ancestor that allows branching. The generation terminates if the focused node has no parents.
- (4) Search loop target. This action indicates that a new ring will be formed, and the model should examine the closest ancestor of the focused node to see whether it is a suitable target during the ring closure. The network can generate this action multiple times until a suitable target is found for ring closure.

- (5) Start loop. This action happens after a “search loop target” action when the appropriate target of ring closure is found. In this action, the model determines the size of the ring. After this action, a series of “append” actions should be issued by the model to complete the ring formation.
- (6) Close loop. This action happens after all ring atoms have been generated, and the model is ready to connect the ring to the target atom determined in the “search loop target” step. The model decides the type of bond used to close the ring during this action.

The process of molecule generation can be represented using a finite state machine, as shown in Figure S3. A full path for generating an example molecule is shown in Figure S4.

A major difference between the generation scheme proposed in this work compared with the previous version of DeepLigBuilder<sup>S4</sup> is its emphasis on ring generation. Before generating explicit ring structures, DeepLigBuilder+ will first determine the size of the ring, as well as the location the ring will be closed. This information will help to guide the process of ring generation. It will also help to avoid problems when the user changes the synthon dataset (to be discussed in the next section, also see Figure S5).

### 1.3 Constraining the model to generate structures inside the synthon database

To ensure synthetic accessibility, the synthons generated by DeepLigBuilder+ must be restricted to the synthon dataset derived from purchasable building blocks. To achieve this goal, most previous methods use reactants as basic units for molecule generation and apply neural networks to parametrize scoring functions that filter the reactant dataset for appropriate candidates at each generation step. In this work, we propose a radically different approach. Instead of adopting a generation scheme based on reactants, we still use atoms as basic generation units, building on the foundation of previous works.<sup>S4,S6</sup> To en-

force constraints on the chemical space, we apply masks on the action space at each step of generation, so that we can ensure that the output topological structure can be found in the synthon dataset.

Next, we show how such action masks can be calculated at each step. First, for each synthon in the synthon database  $s \in \mathcal{S}$ , we represent it as a list of actions that can be used to generate its molecular graph, which is indicated as  $(a_1, \dots, a_T) \rightarrow s$ . The definition of the action space and the generation process follows Section S1.2. Since we only need to constrain the topological structures, 3D action information, such as the position of new atoms, is removed from the action space. For convenience, we refer to such action sequences as trajectories and write them as  $\tau$ . In this way, we convert the synthon dataset into a collection of trajectories  $\mathcal{T}(\mathcal{S}) = \{\tau | \exists s \in \mathcal{S} \text{ s.t. } \tau \rightarrow s\}$ .

To ensure synthons generated by the model lie in  $\mathcal{S}$ , we need to ensure that the generation trajectories lie in  $\mathcal{T}(\mathcal{S})$ . At each step  $t$ , given the generation history  $\tau_t = \tau[1..t-1] = (a_1, \dots, a_{t-1})$ , in order to ensure that the final trajectory will lie inside  $\mathcal{T}(\mathcal{S})$ , we need to make sure that the next action  $a_t$  is inside the following set:

$$a_t \in \mathcal{A}(\tau_t, \mathcal{S}) = \{a | \exists \tau' \in \mathcal{T}(\mathcal{S}) \text{ s.t. } \tau'[1..t] = \tau_t \cdot a\}$$

It is easy to prove that as long as this requirement holds at each step, we can guarantee that the resulting synthon will be inside  $\mathcal{S}$ . In order to efficiently calculate  $\mathcal{A}(\tau_t, \mathcal{S})$ , the trajectories in  $\mathcal{T}(\mathcal{S})$  are organized into a prefix tree. Inside the tree, each node represents a prefix of some trajectory in  $\mathcal{T}(\mathcal{S})$ , and each edge represents an action. During retrieval, we descend the tree to find the node that equals  $\tau_t$ , and then collect all its outgoing edges. It can be seen that those edges form the set  $\mathcal{A}(\tau_t, \mathcal{S})$ . In this way, we can construct action masks at each step to ensure that the resulting synthon can be found in the synthon dataset.

As a method to constrain the chemical space of the generative model, our method has some advantages compared with previous methods:

- (1) The complexity of generating each synthon does not scale with the size of the synthon dataset. Searching inside the prefix tree has an average cost of  $O(L)$ , where  $L$  is the average number of steps required to generate a synthon. Other approaches generally require a full scan of the reactant dataset, which has more limited scalability for larger synthon databases. Constructing the prefix tree will cost  $O(LN)$ , where  $N$  is the size of the synthon, but we only need to construct the tree once, and it can then be reused for subsequent generation tasks.
- (2) Our method only constrains the 2D (topological) structure of molecules, while the 3D coordinates are generated by the neural network. This eliminates the need of building a 3D fragment database, as done in several previous works.<sup>S7,S8</sup> Such approaches may cause some technical issues. First, enumerating 3D conformers will significantly increase the size of the fragment dataset, especially when the dataset contains large flexible structures. Second, the conformation of a fragment depends on its environment, and enumerating its conformation in isolation may result in inaccurate results when the fragment is attached to another molecule.

Some practical issues need to be considered when applying this method:

- (1) There are generally multiple ways to generate a molecular structure. To reduce complexity and computational cost, we follow the approach in previous works,<sup>S4,S6</sup> which uses a depth-first, canonically ordered way to generate molecules. In this way, a molecular graph will correspond to exactly one trajectory, when the starting atom for generation is given. To make the model more flexible, we allow multiple starting points for the generation as in our previous work.<sup>S4</sup>
- (2) When using the proposed method to constrain the chemical space, there may be issues related to ring conformation when the synthon dataset is changed without model re-training. An illustrative example is given in Figure S5. To alleviate this problem, we

adopt a more refined ring-generation scheme, which allocates the size and location of the ring before its structures are generated, as discussed in the previous section.

## 1.4 Network architecture

In this section, we give a detailed description of the neural network architecture. We first describe the inputs required by the network. Then, we show how the inputs are embedded before feeding to the neural network. Next, we detail the architecture of the neural network. Finally, we demonstrate how the output features from the transformer are used to generate the action at each step with a MADE-based policy network.

### 1.4.1 Input features

The model receives previously generated synthons as inputs, as well as shape and pharmacophore information for structure-based generation tasks.

**Graph inputs** All graph-related inputs, including previously generated synthons and the intermediate synthon structures, are represented as their generation trajectories  $\tau$ . This acts as a sequence-based representation of molecular graphs, similar to the concept of a “sentence” in NLP tasks. Each action in the sequence corresponds to a “token” or “word” in the sentence. The following information is included in each token:

- (1) The current step id ( $t$ );
- (2) Action performed at this step, including the action type ( $act_t$ ) and the type of new bonds added ( $nbt_t$ );
- (3) Information of the focused node after the action is applied, such as its index ( $id_t$ , ordered based on the step each atom is generated), element type ( $el_t$ ), formal charge ( $fc_t$ ), and the number of explicit hydrogens ( $neh_t$ ) attached. Information about whether the

node allows for branching ( $b_t$ ) or whether the node can act as a target for ring closure is also included ( $r_t$ ).

- (4) If a ring is being generated, we also input the expected size of the ring ( $rs_t$ ) and the expected target for ring closure ( $rt_t$ ).

In addition to the information above, each token is attached with a 3D coordinate frame ( $\mathbf{o}_t, \mathbf{R}_t$ ) using the method developed in our previous work.<sup>S4</sup> Those frames have several functionalities.

- (1) The coordinates of newly generated atoms are defined under those frames. The spherical coordinate values of the local frames correspond to bond lengths, bond angles, and torsion angles.
- (2) Those frames are used in the IPA modules to communicate 3D information between the tokens.
- (3) Those frames are used to define the relative 3D positional embeddings between tokens (to be discussed below).

Besides input features for each token, we also include features for each action pair as relative embedding to increase the performance of the model. Those pair features include:

- (1) The topological distance between focused atoms at each step ( $top_{tt'}$ ).
- (2) The distance between the focused atoms in the spanning tree induced by the generation trajectory ( $tree_{tt'}$ , recall descriptions in Section S1.2).
- (3) The relative 3D positions between coordinate frames attached to each action ( $\Delta \mathbf{x}_{tt'}$ ). Specifically, for the action pair ( $a_t, a_{t'}$ ), we first calculate the displacement between the origins of each frame and then transform the coordinate values to the local coordinate frame attached to  $a_i$ .



**Pharmacophore inputs** The input pharmacophore model can be represented as a sequence of individual pharmacophore features, with definitions adopted from Align-it.<sup>S9</sup> Each pharmacophore  $p$  contains information about its type ( $pt_p$ ) and radius ( $pr_p$ ). We use the Euclidean distances ( $pd_{pp'}$ ) between pharmacophore pairs ( $p, p'$ ) as relative positional embeddings.

In the decoder, we need to communicate between the pharmacophore model and the synthon structure. Therefore, we feed the model with the following information about the 3D relationship between each pharmacophore-action pair:

- (1) The position of each pharmacophore in the local coordinate system attached to each action ( $\Delta\mathbf{x}_{pt}$ );
- (2) The direction for each pharmacophore (only HBDs and HBAs) in the local coordinate systems attached to each action ( $\hat{\mathbf{n}}_{pt}$ ).

**Shape inputs** The shape input can originate from known active ligands or directly from the target pocket using programs such as PANTHER.<sup>S10</sup> In both cases, we represent the input shape as a set of 3D spheres. Most previous models use 3D-CNN to encode shape information.<sup>S11</sup> This method is not equivariant and induces additional computational costs. In comparison, DeepLigBuilder+ uses a more compact, SE(3) equivariant representation for 3D shapes based on 3D Zernike coefficients. For an input shape composed of 3D spheres, we can represent it using a 3D scalar function following Grant et al.:<sup>S12</sup>

$$f(\mathbf{x}) = \sum_{i=1}^N p_i \exp(-\alpha_i |\mathbf{x} - \mathbf{x}_i|^2)$$

Where  $\mathbf{x}_i$  is the location of each sphere, and  $p_i$  and  $\alpha_i$  are parameters related to the radius of each sphere. We define the function in the coordinate frame placed in the center of the

spheres  $\mathbf{x}^c = \frac{1}{N} \sum_{i=1}^N \mathbf{x}_i$ . The function is then decomposed as:

$$f(\mathbf{x}) = \sum_{nlm} c_{nl}^m Z_{nl}^m(\mathbf{x})$$

Where  $Z_{nl}^m(\mathbf{x})$  are 3D Zernike polynomials.<sup>S13</sup> In this work, we use a truncated series with  $n \leq 9$ . Those functions are generalizations of Zernike polynomials defined in 2D space and act as the orthogonal basis for 3D functions (defined in a ball with radius 1). Additionally, those coefficients  $\mathbf{c} = \{c_{nl}^m\}_{nlm}$  changes in an equivariant manner when a rotation  $\mathbf{R} \in SO(3)$  is applied to the function  $f$ :

$$f'(\mathbf{x}) = f(\mathbf{R}^{-1}\mathbf{x}) = \sum_{nlm} \sum_{m'} R_{mm'}^l c_{nl}^{m'} Z_{nl}^m(\mathbf{x})$$

Where  $R_{mm'}^l$  are the matrices that can be used to “rotate” the coefficients of the function  $f$ . Those matrices can be efficiently calculated using the methods proposed by Ivanic et al.<sup>S14</sup>

The representation of the shape can then be written as  $(\mathbf{x}^c, \mathbf{c})$ . When feeding into the model, we rotate it into the local coordinate frames of each action  $(\mathbf{x}_t^c, \mathbf{c}_t)$ , and concatenate it with other action features. In other words, the shape information is used by the transformer similar to a positional embedding for each token.

### 1.4.2 Embedding layers

Several types of embedding layers are used for the input information discussed above, including:

- (1) Lookup tables with trainable parameters. This type of layer is used to embed atom, bond, and pharmacophore types, as well as topological distances. The full list of inputs includes  $act_t$ ,  $nbt_t$ ,  $el_t$ ,  $fc_t$ ,  $neh_t$ ,  $b_t$ ,  $r_t$ ,  $rs_t$ ,  $top_{tt'}$ ,  $tree_{tt'}$ , and  $pt_p$ .
- (2) Positional embedding using sine and cosine functions.<sup>S15</sup> This type of embedding is widely used in transformer models to embed position-related data. In this work, we

use it to embed time, position, and distance-related information. The full list includes  $t$ ,  $idx_t$ ,  $rt_t$ ,  $\Delta \mathbf{x}_{tt'}$ ,  $pd_{pp'}$ ,  $\Delta \mathbf{x}_{tp}$  and  $\mathbf{x}_t^c$ .

- (3) Some inputs with continuous representations are input to the model as-is. This includes:  $pr_p$ ,  $\hat{\mathbf{n}}_{pt}$ , and  $\mathbf{c}_t$ .

After the inputs are embedded, for each token (action or pharmacophore) and token pair, we concatenate all input information into a vector and use a linear layer to project the inputs to a predefined dimension, which is then used as transformer inputs. We write the size of the dimension as  $F$  for each token and  $F'$  for each token pair. In this work, we have  $F' = \frac{F}{2}$  and two values  $\{512, 256\}$  are experimented for  $F$ .

### 1.4.3 The transformer architecture

The transformer is responsible for processing the input features to generate a state embedding at each step. Later, this state embedding will be used by the policy network for action sampling. The transformer consists of multiple encoders responsible for processing different inputs, and a decoder used to generate the state embedder. The decoder and encoders are composed of transformer layers, each containing one or more attention layers and a tokenwise dense layer. The attention and dense layers are wrapped inside residue blocks.

**Attention layers** Two types of attention layers are used in this work. The first is the widely used scaled dot-product attention (SDPA),<sup>S15</sup> with additional relative positional bias. Given the features of the source sequence  $\{\mathbf{h}_i^s\}_{i=1}^{l_s}$ , the target sequence  $\{\mathbf{h}_i^t\}_{i=1}^{l_t}$ , and the source-target token pairs  $\{\mathbf{h}_{ij}^p\}_{i=1, \dots, l_t}^{j=1, \dots, l_s}$ , the attention layer performs the following operations to calculate the output feature  $\{\mathbf{h}'_i\}_{i=1}^{l_t}$  for each target token:

$$[\mathbf{k}_j^h, \mathbf{v}_j^h]_{h=1}^H = \text{Linear}_{kv}(\mathbf{h}_j^s), [\mathbf{q}_i^h]_{h=1}^H = \text{Linear}_q(\mathbf{h}_i^t), [b_{ij}^h, \mathbf{z}_{ij}^h]_{h=1}^H = \text{Linear}_p(\mathbf{h}_{ij}^p)$$

$$a_{ij}^h = \text{softmax}_j \left( \frac{1}{\sqrt{d}} \mathbf{q}_i^h \cdot \mathbf{k}_j^h + b_{ij}^h \right)$$

$$\mathbf{h}'_i = \text{Linear}_{out} \left( \left[ \sum_{j=1}^{l_s} a_{ij}^h \mathbf{v}_j^h, \sum_{j=1}^{l_s} a_{ij}^h \mathbf{z}_{ij}^h \right]_{h=1}^H \right)$$

where  $i = 1, \dots, l_t$ ;  $j = 1, \dots, l_s$ ;  $h = 1, \dots, H$

$H$  denotes the number of attention heads, which is set to be 16 in this work.  $d$  is the dimension of each query, key, or value vector, which is set to be  $d = \frac{F}{H}$ , the  $[\cdot]$  operator represents concatenation or unpacking respectively when it appears in the right or left side of the equations.

The second type of attention is invariant point attention (IPA), initially proposed in AlphaFold2.<sup>S16</sup> Similar to SDPA, we first calculate vector-based queries for the target sequence, as well as the keys and values for the source sequence:

$$[\mathbf{k}_j^h, \mathbf{v}_j^h]_{h=1}^H = \text{Linear}_{kv}(\mathbf{h}_j^s), [\mathbf{q}_i^h]_{h=1}^H = \text{Linear}_q(\mathbf{h}_i^t), [b_{ij}^h, \mathbf{z}_{ij}^h]_{h=1}^H = \text{Linear}_p(\mathbf{h}_{ij}^p)$$

where  $i = 1, \dots, l_t$ ;  $j = 1, \dots, l_s$

Different from SDPA, IPA also calculates keys, queries, and values based on 3D points:

$$[\vec{k}_i^{ph}, \vec{v}_i^{ph}]_{p=1, \dots, P}^{h=1, \dots, H} = \text{Linear}_{kv}^{3D}(\mathbf{h}_i^s), [\vec{q}_j^{ph}]_{p=1, \dots, P}^{h=1, \dots, H} = \text{Linear}_q^{3D}(\mathbf{h}_j^t)$$

where  $i = 1, \dots, l_t$ ;  $j = 1, \dots, l_s$

Where  $P$  is the number of points for each attention head and is set to be 8 in this work. Those points are defined on the local coordinate system attached to each token and can be transformed into the global coordinate system as:

$$\vec{k}_j^{ph} = \mathbf{R}_j^s \vec{k}_j^{ph} + \mathbf{o}_j^s, \vec{v}_j^{ph} = \mathbf{R}_j^s \vec{v}_j^{ph} + \mathbf{o}_j^s, \vec{q}_i^{ph} = \mathbf{R}_i^t \vec{q}_i^{ph} + \mathbf{o}_i^t$$

where  $i = 1, \dots, l_t$ ;  $j = 1, \dots, l_s$ ;  $h = 1, \dots, H$ ;  $p = 1, \dots, P$

Where  $\{(\mathbf{o}_i^t, \mathbf{R}_i^t)\}_{i=1}^{l_t}$  and  $\{(\mathbf{o}_i^s, \mathbf{R}_i^s)\}_{i=1}^{l_s}$  are coordinate frames attached to each source and target tokens. Attention maps are then calculated as:

$$a_{ij}^h = \text{softmax}_j(w_L(\frac{1}{\sqrt{d}}\mathbf{q}_i^h \cdot \mathbf{k}_j^h + b_{ij}^h - \frac{\gamma^h w_C}{2} \sum_{p=1}^P |\vec{q}_i^{ph} - \vec{k}_j^{ph}|^2))$$

where  $i = 1, \dots, l_t$ ;  $j = 1, \dots, l_s$ ;  $h = 1, \dots, H$

In which  $w_L = \sqrt{\frac{1}{3}}$  and  $w_C = \sqrt{\frac{2}{9P}}$ . The values are then used to calculate the output features:

$$\mathbf{f}_i^h = \sum_{j=1}^{l_s} a_{ij}^h \mathbf{v}_j^h$$

$$\tilde{\mathbf{f}}_i^h = \sum_{j=1}^{l_s} a_{ij}^h \mathbf{z}_{ij}^h$$

$$\vec{f}_i^{hp} = (\mathbf{R}_i^t)^{-1}(\sum_{j=1}^{l_s} a_{ij}^h \vec{v}_j^{ph} - \mathbf{o}_i^t)$$

$$\mathbf{h}'_i = \text{Linear}_{\text{out}}([\mathbf{f}_i^h, \tilde{\mathbf{f}}_i^h, [\vec{f}_i^{ph}]_{p=1}^P]_{h=1}^H)$$

where  $i = 1, \dots, l_t$ ;  $h = 1, \dots, H$ ;  $p = 1, \dots, P$

Note that compared with the original implementation, we do not include the norm of  $\vec{f}_i^{hp}$  in the input of the linear projection. SDPA and IPA are used in different situations in the transformer network. The encoder for previous synthons uses IPA. In the decoder, self-attention layers and outer-attention layers with previous synthons use IPA. The encoder for pharmacophores and the decoder outer-attention layers with pharmacophores use SDPA.

**The token-wise dense layers (MLP layers)** MLP layers consist of two dense layers, each with a normalization-activation-linear architecture. In this work, we use layer normalization<sup>S17</sup> and ELU<sup>S18</sup> as activation units. The number of hidden features is set to be

2*F*.

**Transformer layers** The attention layers and MLP layers are composed of transformer layers that are later stacked into the encoder and decoder networks. Each transformer layer in the encoder consists of one attention layer and one MLP layer. Each transformer layer in the decoder consists of two attention layers, one for self-attention and the other for outer attention, and an MLP layer. The attention and MLP layers are all wrapped inside residual blocks.

**Encoders, decoders, and the transformer network** Multiple transformer layers are stacked to form the encoder and decoders. For unconditional generation tasks, we use 6 blocks for the encoder of previous synthons and 6 blocks for the decoder. For structure-based generation tasks, the model also receives shape and pharmacophore-based information, which uses 3 more encoder and decoder layers for processing. A shallow configuration is also experimented with in unconditional generation tasks, as a way to demonstrate the performance using different network scales. In this configuration, the encoder and the decoder each uses 3 blocks of transformer layers.

Two versions of geometric transformers are developed in this work. An unconditional transformer is used to access the ability of this method to generate drug-like, geometrically valid molecules with high synthesizability. A conditional one, which receives user-provided pharmacophores and shapes as extract inputs, is used as the rollout policy to accelerate MCTS in SBDD problems.

#### 1.4.4 The policy network

Using the state embedding generated by the transformer network, a policy network is then applied to generate the action for the next step. Before specifying the architecture of this network, we need to first define the action space. Two types of decisions need to be made at each step of the generation. The first one relates to the topological structure of the molecule,

including the type of action to be carried out, the type of the new atom and bond, the size of the new ring, etc. The second one relates to the 3D molecular structure, that is the position of the new atom.

For topological decisions, we iterate through the synthon dataset to collect the actions that are needed to produce all the synthon structures. This result in the topological action space  $\mathcal{A}^{\text{topo}}$ . For 3D actions, we write the location of the new atom added to each step in the local spherical coordinate system attached to the focused node  $(r, \theta, \phi)$ . We then discretize  $r$ ,  $\theta$  and  $\phi$ , each using two integers. Take the  $\phi$  coordinate for example. We first split its domain  $(-\pi, \pi]$  into  $N_1$  equal-sized intervals  $(-\pi + \frac{2\pi}{N_1}i, -\pi + \frac{2\pi}{N_1}(i+1)]$ ;  $i = 1, \dots, N_1$ , and find the one containing the coordinate value  $\phi$ . The interval found is named  $\phi^{\text{crude}}$ . To achieve further precision,  $\phi^{\text{crude}}$  is then divided into  $N_2$  smaller chunks. We find the one containing  $\phi$ , and name it  $\phi^{\text{refined}}$ . Similar procedures are applied for  $r$  and  $\theta$ .

Following the definition above, we can now write the action as:

$$a = (a^{\text{topo}}, r^{\text{crude}}, r^{\text{refined}}, \theta^{\text{crude}}, \theta^{\text{refined}}, \phi^{\text{crude}}, \phi^{\text{refined}})$$

where  $a^{\text{topo}} \in \mathcal{A}^{\text{topo}}$ ;

$$r^{\text{crude}}, \theta^{\text{crude}}, \phi^{\text{crude}} \in \{1, \dots, N_1\}$$

$$r^{\text{refined}}, \theta^{\text{refined}}, \phi^{\text{refined}} \in \{1, \dots, N_2\}$$

In this work,  $N_1$  is set to be 30 and  $N_2$  to be 32. The task of the policy network is to parametrize the distribution of  $a$  using the neural network:  $p_\eta(a|\mathbf{h})$ , where  $\eta$  is the parameter of the network, and  $\mathbf{h}$  is the state embedding. To efficiently model the joint distribution of discrete variables in  $a$ , we factorize  $p_\eta$  autoregressively and use MADE (masked autoencoder for density estimation) as the model architecture. The network contains 3 layers and 630 hidden units for each layer.

The general idea of the policy network is similar to the previous version of DeepLig-

Builder.<sup>S4</sup> The major difference is that we now use a discretized action space for the 3D positioning of new atoms. Previously, we found that modeling the continuous distribution of atom positions faces numerical issues, and proposed SoftMADE to address those issues. However, SoftMADE works by adding noise to the 3D coordinates, which reduces the accuracy of the model. Here in DeepLigBuilder+, we use a two-step discretization process, which ensures the precision of the distribution and can also avoid numerical instabilities in continuous distributions.

## 1.5 Dataset and network training

### 1.5.1 Training the unconditional model

We use a dataset containing drug-like molecules randomly assembled using the building blocks in the Enamine global stock as the training set. The assembling process follows a step-wise procedure, which is initialized with a random building block sampled from the dataset. At each step, the possible reactions that can happen to the molecule are enumerated. The reaction type is then randomly selected from the results, and the next reactant is sampled from the building block set based on the selected reaction type. Molecules are assembled with three reactants combined using two reaction steps. Several filters are applied to obtain drug-like molecules, including (1) Lipinski’s rule-of-5 (Ro5),<sup>S19</sup> (2) Veber’s rule,<sup>S20</sup> (3) PAINS patterns,<sup>S21</sup> and (4) a QED<sup>S22</sup> threshold of 0.5. After this process, we obtained approximately 1 million (974,917) molecules, with 4/5 of which used as the training set, and the rest used for validation and testing. The 3D conformers of those molecules are generated using RDKit, by first using ETKDG to embed the molecules into 3D space, and then optimizing them using MMFF94s. To create more stable conformers, at most 10 conformers are generated for each molecule, and the one with the lowest energy is used for model training. Finally, those molecular structures are converted to synthons and subsequently transformed into generation trajectories to train the unconditional transformer.

The network is implemented using PyTorch, and Adam is used for model optimization,<sup>S23</sup>



with a linear learning rate warm-up of one epoch to 0.001, followed by an exponential learning rate decay. The decay rate is 0.01, and several decay frequencies are experimented with (see Table S1). The batch size is set to 1024, and the model is trained for 100 epochs using 4 A100 GPUs, which may take 1-2 days to complete.

To train the shape and pharmacophore-conditioned model, a dataset of input-output pairs is constructed. First, we extracted a set of ligand-based pharmacophore models and shapes from the 3D ligands in the PDBBind 2020 dataset.<sup>S24</sup> We use PDBBind as the data source due to its ligand diversity. It not only contains drug-like ligands, but also metabolites, peptides, fragments, and other types of ligands that lack drug-likeness but are still frequently used in pharmacophore extraction and interaction analysis. In this way, we can increase the diversity of the pharmacophore and shape inputs. Note that we do not use the protein structure and bioactivity values inside the PDBBind dataset, therefore the extracted information is fully unlabeled. Future research may also consider that information to improve the quality of the extracted pharmacophores.

An overall 12,456 pharmacophores and shapes are extracted. Next, we align the assembled molecules to the extracted pharmacophores and filter those with a good match to form the training set. This process requires  $974,917 \times 12,456$  3D alignment operations, and due to its time cost, we utilize an approach based on sequential filtering:

- (1) First, we perform similarity calculation based on USRCAT fingerprints, and filter the top 10,000 most similar molecules to each pharmacophore and shape query. Since USRCAT similarity does not involve 3D alignment, it can be carried out with high efficiency inside GPU;
- (2) Next, we perform 3D alignments between the  $10,000 \times 12,456$  pairs of molecules and queries based on 3D shape. The shapes are represented as a combination of 3D Gaussian functions, as described previously,<sup>S12</sup> each "colored" with a pharmacophore type assigned using a set of SMARTS patterns defined in RDKit. PCA is then performed on the point sets to obtain the principle axes, and those axes are aligned to form the initial

pose. 4 candidate poses are created by rotating  $180^\circ$  around each axis. A gradient-based optimization process is then used to tune the rotation and translation to achieve the best overlap between two shapes. The alignment process is accomplished using an in-house PyTorch program. Shape similarity is computed using the aligned pose, and the top 100 most similar molecules are retained for each pharmacophore-shape query.

- (3) After shape-based alignment and filtering, a more refined pharmacophore-based filtering is used to further enrich molecule-query pairs with a good match. At this step, we retain the top 10 most similar molecules for each pharmacophore and shape-based query.

The filtering process described above creates a dataset containing  $10 \times 12,456 = 124,560$  input-output pairs for model training. When training the conditional model, we use the pre-trained unconditional model as the base model and add pharmacophore and shape-related layers at the tail of the transformer. To avoid overtraining, only the parameters of the newly added layers are allowed to change. The training is performed for 160 epochs and the learning rate decay is performed for every 30 steps. Other hyperparameters for training the conditional model are similar to that used to train its unconditional counterpart.

## 1.6 Monte Carlo tree search

Monte Carlo tree search is a widely used technique in reinforcement learning which finds promising solutions for a given problem by strategically expanding the search tree. In this work, we combine MCTS with the pharmacophore and shape-conditioned transformer for the design of synthesizable 3D molecules inside a given pocket. In order to search for promising molecular structures, MCTS maintains a look-ahead tree  $\mathcal{T}$  and iteratively builds  $\mathcal{T}$  using four steps: selection, expansion, simulation, and backpropagation. DeepLigBuilder+ uses a variant of MCTS that includes several modifications to better suit it to the 3D molecule generation tasks. In this section, we first describe the data structure of the look-ahead tree

$\mathcal{T}$ , then discuss how the tree is updated at each step, and finally specify the details of the hyperparameters used during MCTS runs.

The look-ahead tree in MCTS is used to store the history of previous visits, with each node representing an intermediate state during molecule generation, and each edge representing an action carried out at each step. In DeepLigBuilder+, we introduced several custom modifications in the data structure of nodes and edges:

- (1) Edges in the tree contain topological and 3D actions applied to the molecular graph at each step. The 3D action is discretized using the method introduced in Section 1.4.4. Note that the edge only stores the value of the  $\phi$  coordinate, or torsion angle. This is because the bond lengths  $r$  and bond angles  $\theta$  are largely determined by the bond types and ring sizes, which are already stored in the topological actions.
- (2) The torsion angles of new atoms are stored in a coarse-grained form, that is  $\phi^{\text{crude}}$ . In this way, nodes in  $\mathcal{T}$  now represent sets of molecule structures with similar 3D conformations. This has a similar effect of clustering intermediate states using the torsion fingerprint.

At each step of MCTS, the following operation are carried out consecutively:

- (1) The selection operation, which chooses a promising state from the tree based on its estimated value function. We follow MENTS<sup>S25</sup> and use E2W (Empirical Exponential Weight) to generate the selection policy. As mentioned that each node represents a cluster of states with the same topological structure and similar 3D conformation. We randomly select one of the states from the cluster;
- (2) The expansion operation, which enumerates all possible actions that can be carried out given a state. In practice, we found that although the allowed action space for the 3D generative model is large, generally only a small subset of actions will be selected by the model. Based on this observation, we first perform multiple independent sampling

of actions given the state selected using the transformer, and cluster the actions based on their topological action and torsion angle, as described previously. This procedure is similar to pruning branches in the search tree with a small probability of being chosen by the transformer;

- (3) The simulation operation, in which a full rollout is performed based on the selected state, and the results are evaluated using the Smina scoring function. Note that all new states created in the expansion operation are used to perform the rollout, which acts as a form of leaf-level parallelism.<sup>S26</sup> Additionally, all subsequent actions generated at each rollout are added to the tree, which may help to reduce the instability during the tree search.

Compared with the previous version of DeepLigBuilder, during the rollout, we use a shape and pharmacophore-conditioned generative model

When evaluating the generated outcome, DeepLigBuilder+ uses a soft version of the Smina score as the reward function:

$$R(m) = \frac{\text{softplus}(-S(m)) + \sum_{i=1}^3 \text{softplus}(-S(s_i))}{2}$$

Where  $m$  is generated molecule,  $s_i$ ,  $i \in \{1, 2, 3\}$  are the synthons fragments composed of the molecule,  $S(\cdot)$  is the Smina score (evaluated directly without minimization), and  $\text{softplus}(x) = \ln(1 + \exp(x))$ . Adding softplus to the equation helps to reduce large penalties from the clashes with the pocket, making the reward function softer.

- (4) The backtracking operation, in which the calculated rewards are used to update the Q value estimates for each edge. Following MENTS, we use the soft-bellman backup as the operator to update the Q values.

The number of rollout steps for each case study is set to 100. To fully utilize GPU resources, tree-level, root-level, and leaf-level parallelism are applied.<sup>S26</sup> During selection,

an overall of 16 nodes is selected at once for simulation. Also, 20 trees are constructed independently for each case study. During expansion, 32 actions are sampled from the full action space for clustering, and those actions are all used to form updated states for rollout. There are two major parameters controlling the balance between exploration and exploitation in MENTS,<sup>S25</sup> the temperature parameter  $\tau$  and the exploration parameter  $\epsilon$  in E2W. In this work, we have  $\tau = 0.25$  and  $\epsilon = 0.05$ . The MCTS program uses one NVIDIA 3070 graphics card with 1 CPU core.

## 1.7 Model evaluation

Several evaluations are performed to examine the performance of DeepLigBuilder+ in different aspects.

### 1.7.1 The unconditional generation tasks

For the unconditional model, we investigate whether it can generate drug-like molecules with high-quality 3D structures. To this end, a dataset containing molecules randomly assembled from the building blocks without drug-likeness filters is constructed as the target of comparison, and the following evaluation metrics are employed:

- (1) Metrics related to the molecular properties. For each molecule, a series of 2D or 3D properties are calculated, including molecular weight, LogP, QED, the number of hydrogen bond donors and acceptors, the number of rotatable bonds, total and polar solvent accessible surface areas, and the radius of gyration. The distributions of those properties are then compared between the generated molecules, the assembled molecules, and the test set molecules. To make the comparison, the mean and standard deviation values are calculated for each property in each dataset. We also use a metric calculated using the RMSD between mean and standard deviation values for a quantitative measurement:  $W = \sqrt{(\mu_1 - \mu_2)^2 + (\sigma_1 - \sigma_2)^2}$ . Mathematically, this

metric is equivalent to the Wasserstein distance between Gaussian approximations of two distributions.

- (2) For a more quantitative measurement of whether the model correctly constructed the drug-like chemical space of synthesizable molecules, we evaluate the MMD<sup>S27</sup> between generated molecules and test set molecules using 2D (morgan) and 3D (USRCAT) fingerprints. MMD, which stands for the maximum mean discrepancy, is a widely used technique for evaluating the differences between distributions, and are applied in several previous works for the evaluation of molecule generative models.<sup>S4,S28</sup> MMD can be calculated as follows:

$$\text{MMD}_u^2(X, Y) = \frac{1}{m(m-1)} \sum_{i \neq j} k(x_i, x_j) + \frac{1}{n(n-1)} \sum_{i \neq j} k(y_i, y_j) - \frac{2}{mn} \sum_{ij} k(x_i, y_j)$$

Where  $X = \{x_i\}_{i=1}^m$  and  $Y = \{y_i\}_{i=1}^n$  are two datasets to be compared.  $k$  is the kernel function based on either the Morgan or USRCAT fingerprint.

- (3) To evaluate the quality of 3D structures, we first examine the quality of local geometries of generated molecules. Similar to the previous work,<sup>S4</sup> we compare the distribution of torsion angles between generated molecules and the test set molecules. The environments are described using torsion SMARTS patterns by Schärfer et al.<sup>S29</sup> The difference between torsion angle distributions is quantized using MMD. We use the cosine values of torsion angle difference as kernel function when calculating the MMD.
- (4) To further assess the quality of generated conformers by the model, we optimize each generated molecule using the MMFF94s force field and calculate the RMSD value between conformers before and after the optimization. To provide a context of the model’s performance, we also perform this evaluation on conformers generated using the ETKDG<sup>S30</sup> method. This method is initially proposed as a faster alternative for forcefield-based conformation optimization.

### 1.7.2 The structure-based generation tasks

When evaluating the performance of DeepLigBuilder+ in structure-based generation tasks, we mainly focus on answering the following two questions:

- (1) Can MCTS help enrich molecules with high docking scores?
- (2) Can shape-based and pharmacophore-based conditional rollout policy help MCTS to discover better results faster?

A series of ablation studies are performed to answer those two questions. First, in terms of the benefit of MCTS-based sampling, we compare the distribution of Smina docking scores for molecules generated with or without MCTS. When calculating the Smina scores, we first move the generated molecules out of the protein pocket, perform local relaxation for each molecule using the MMFF94s forcefield, and then re-dock the relaxed conformers back into the target pocket using Smina.

To access the benefit of the conditional rollout policy, the following studies are performed:

- (1) We determine whether the conditional model can achieve enrichment in pharmacophore and shape compared with its unconditional counterpart. This question can be answered by examining the distribution of shape and pharmacophore similarity between generated molecules and input queries.
- (2) We investigate whether the extra conditional inputs can help MCTS to achieve faster search speeds. To this end, ablation studies are performed by enabling and then disabling the conditional inputs for the rollout policy. At each MCTS step, we record the reward value for the best molecule found so far. We then compare whether the conditional rollout policy can help MCTS reach solutions with higher rewards faster.

## 2 Supplementary Figures

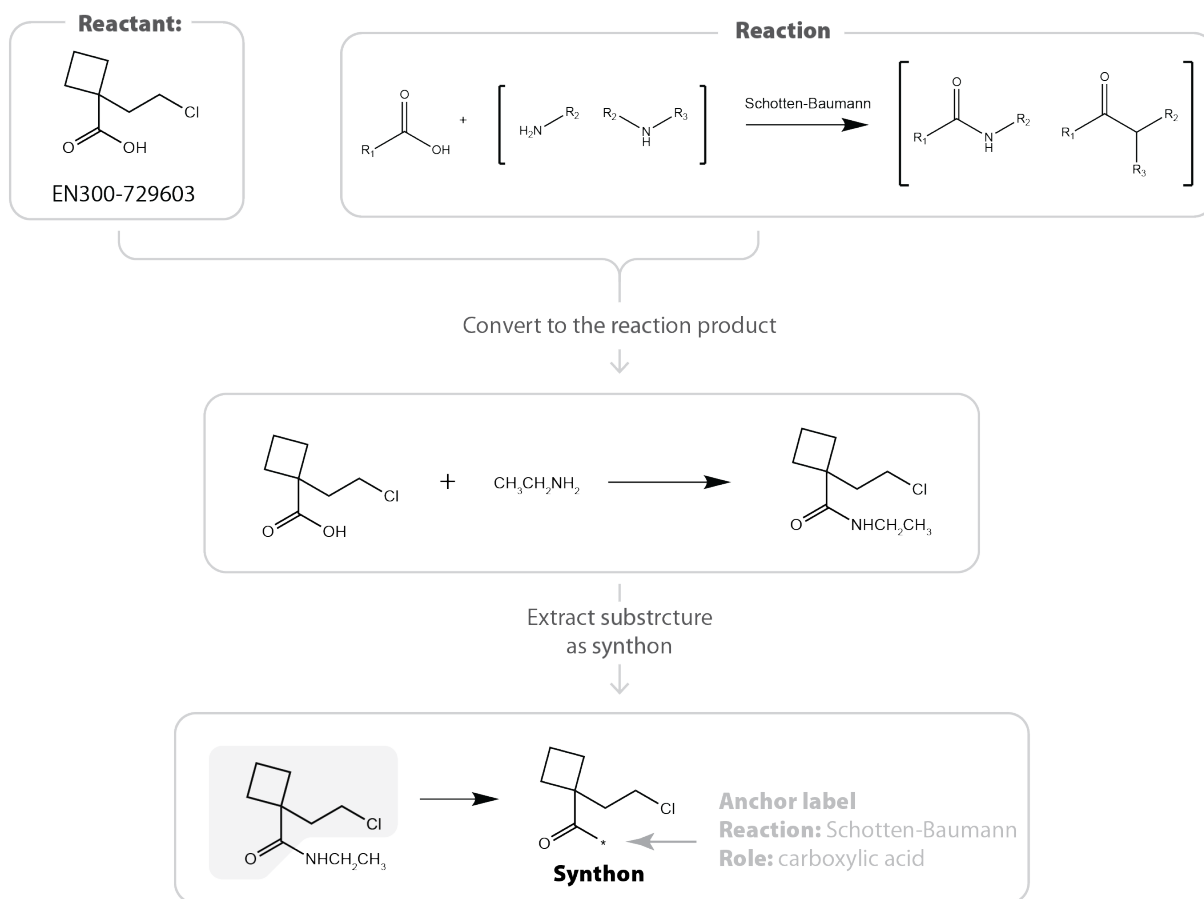


Figure S1: The process of converting a reactant in the building block dataset into a synthon.



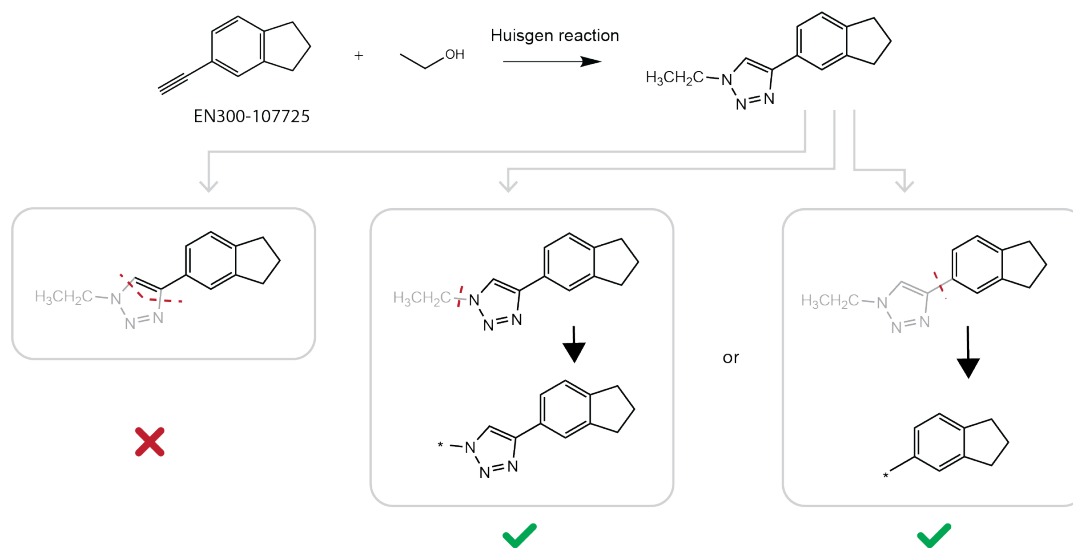


Figure S2: Special treatment is needed when converting reactants to synthons when the reaction involves ring formation.

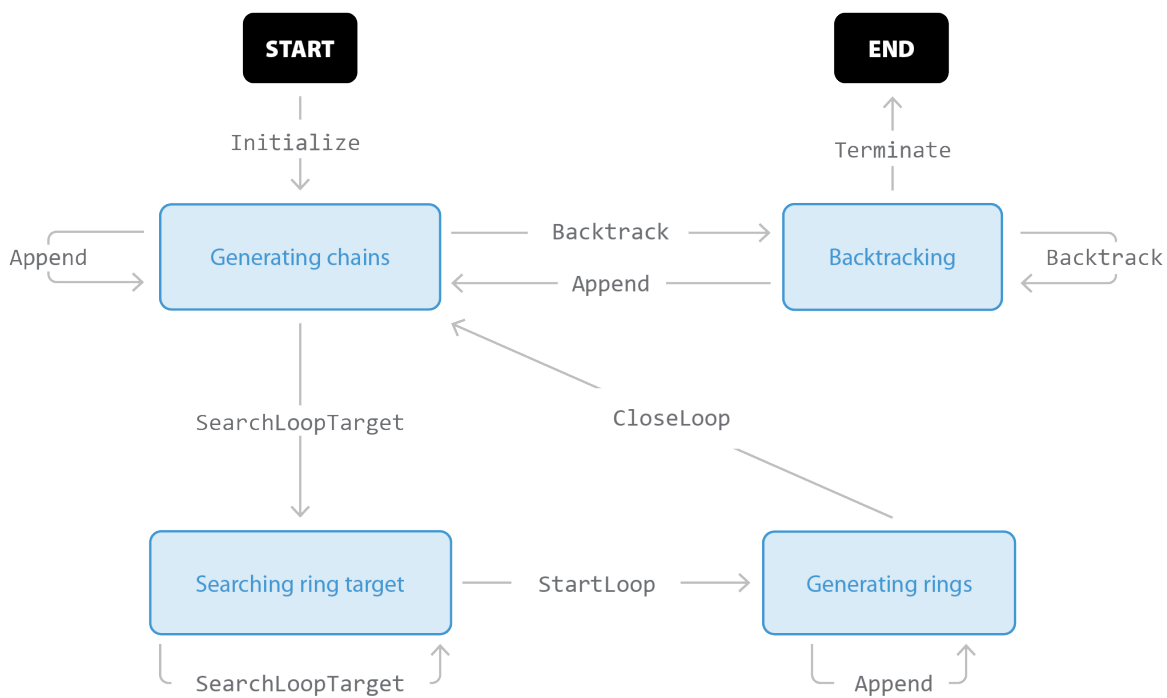


Figure S3: A representation of the molecule generation process using a finite state machine. From the figure, we can see that the model moves back and forth between ring generation (represented as the “searching ring target” state and the “generating ring” state) and chain generation (represented as the “generating chains” state and the “backtracking” state).

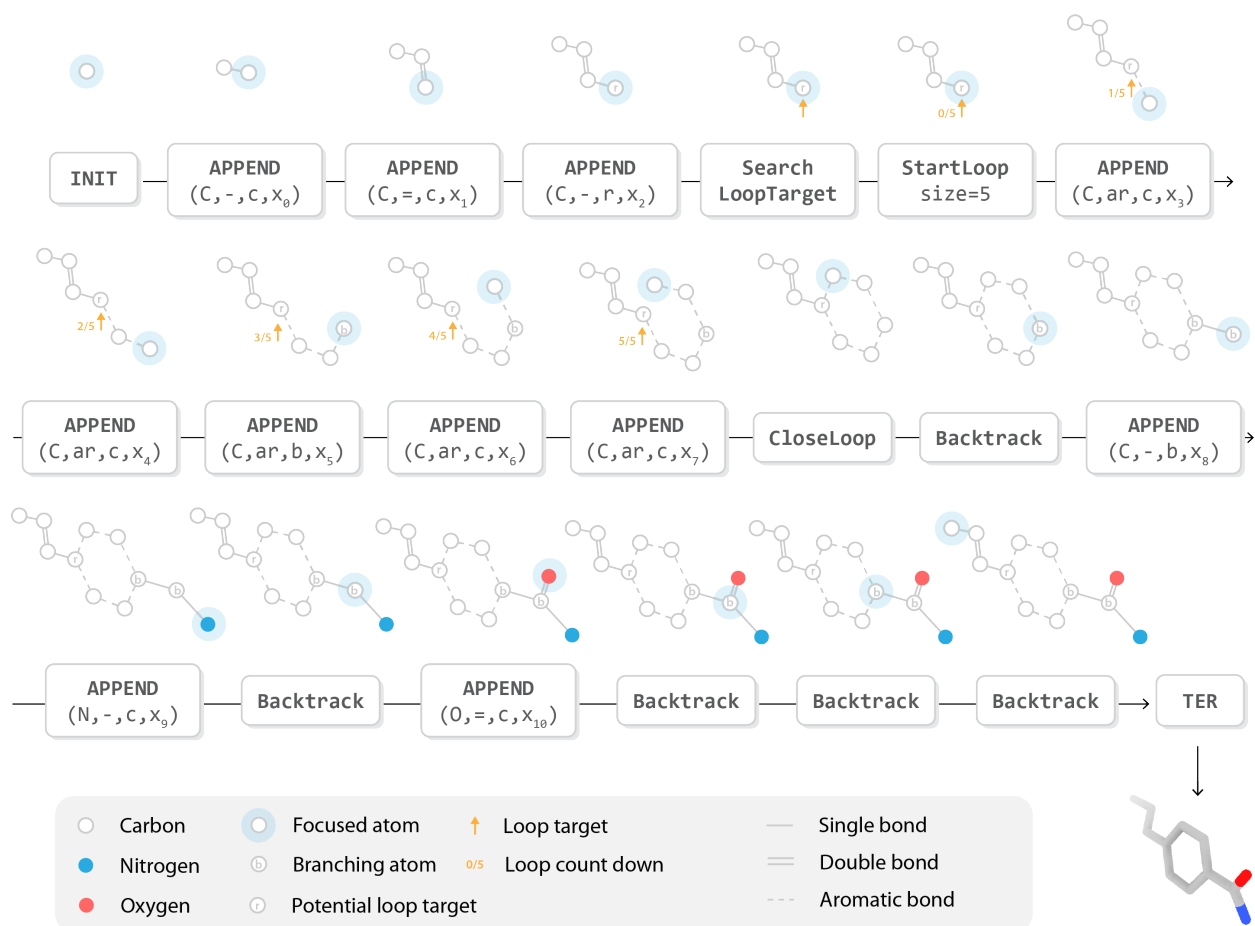


Figure S4: The process of generating a 3D molecule using DeepLigBuilder+

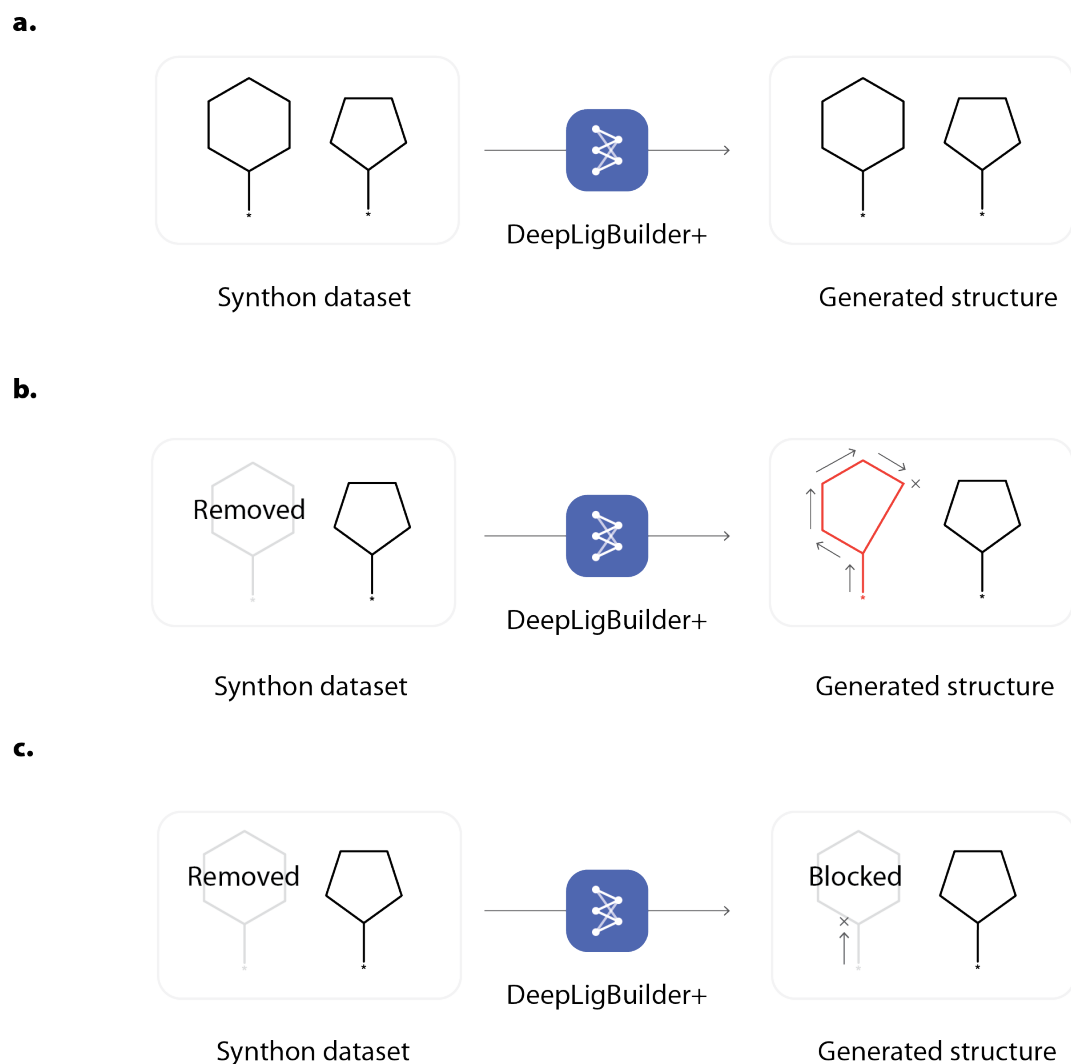


Figure S5: Issues related to ring generation when the synthon dataset is changed, and how the refined ring-based generation scheme can alleviate this problem. **a.** The original synthon dataset, and the structures of generated molecules. **b.** The six-membered ring is removed from the dataset. Without retraining, the model will not acknowledge this change. As a result, the model will still attempt to generate six-membered rings, but the generation will be terminated in advance due to the constraints on available synthons, resulting in problematic structures shown below. **c.** However, if the ring size is determined before generating its structures, the model will acknowledge the change in the synthon dataset, since the action of generating a six-membered ring is masked due to the imposed synthon constraints, resulting in molecule structures with higher quality.

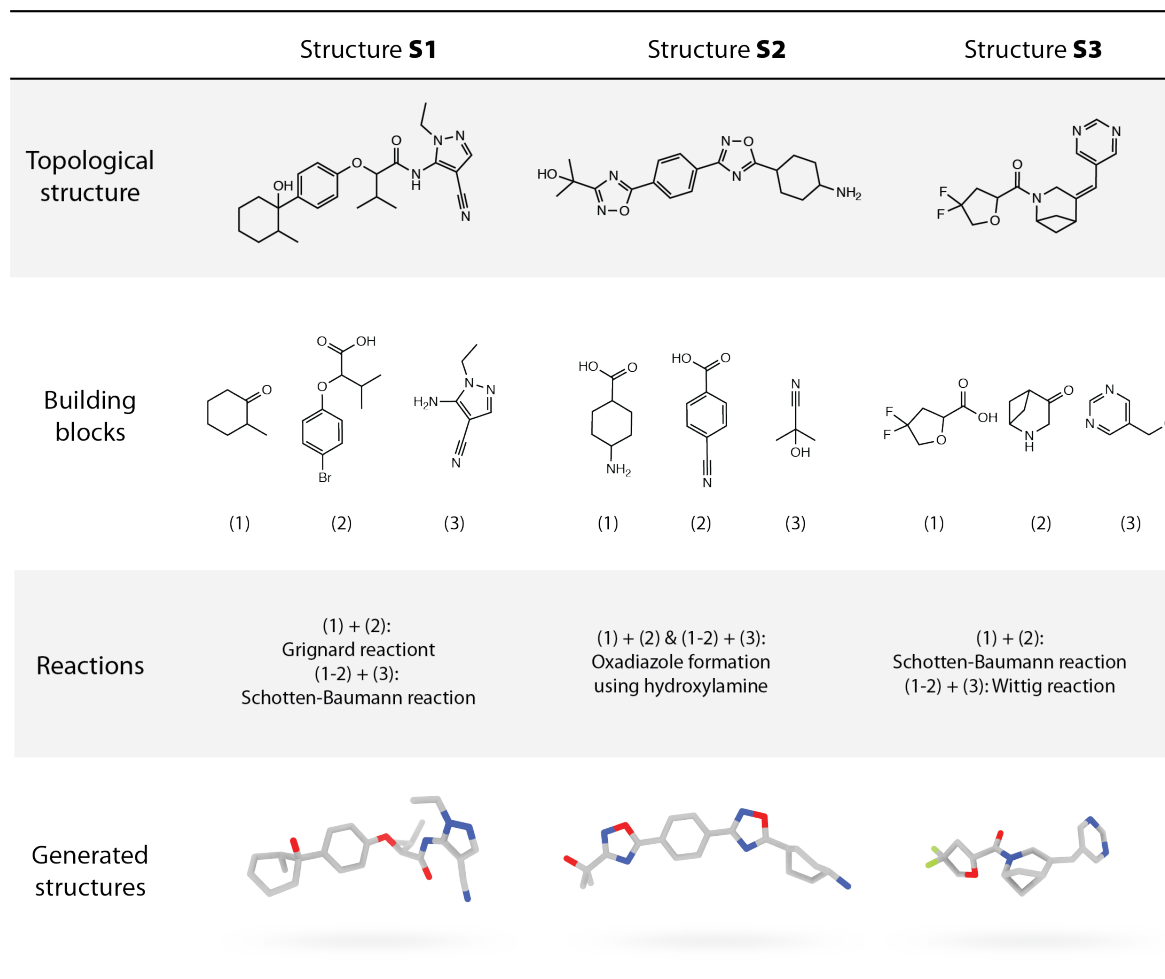


Figure S6: Examples of several generated 3D molecules using the unconditional transformer, along with the building blocks and proposed reactions to synthesize the molecules.

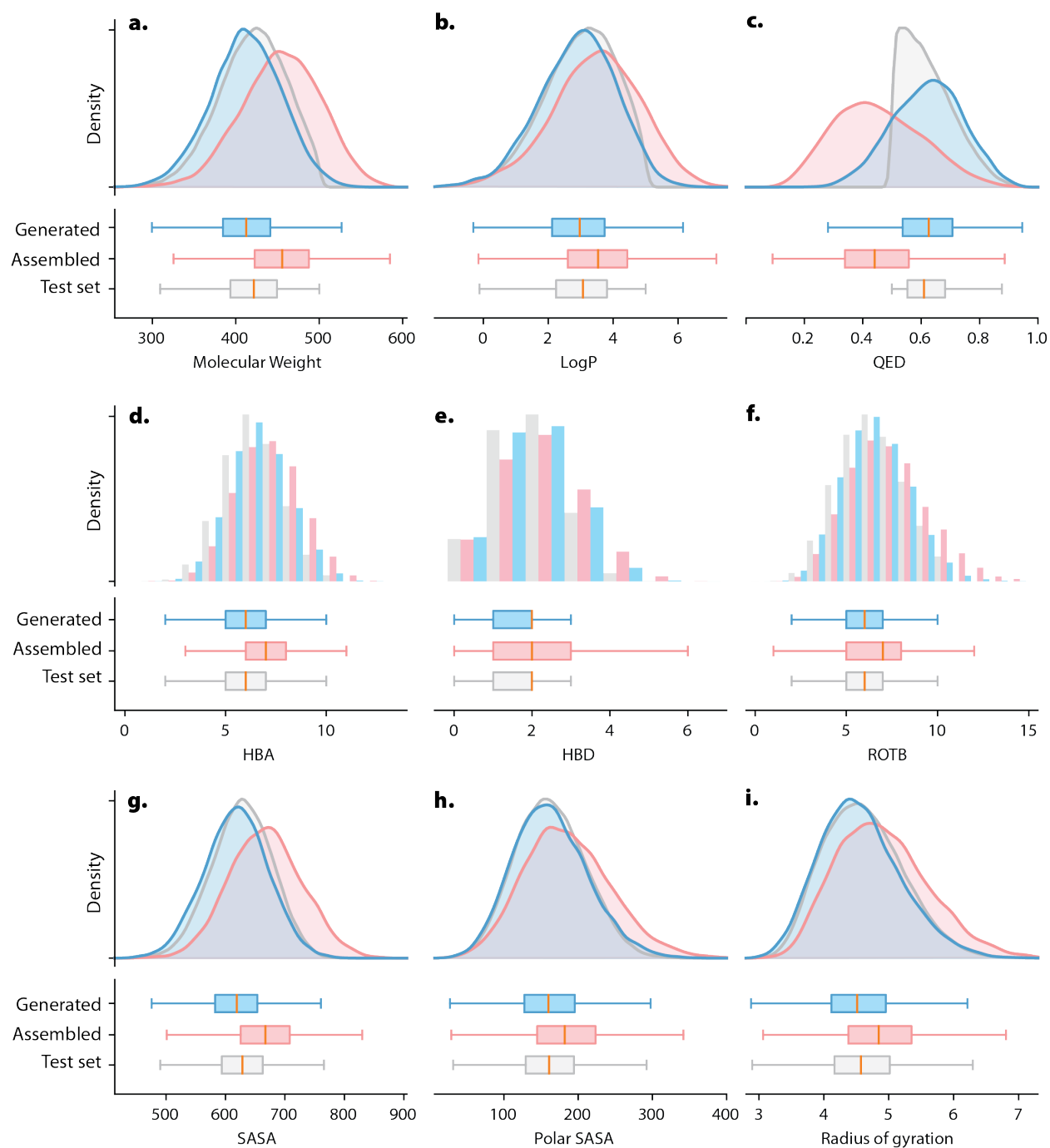


Figure S7: The distribution of 2D and 3D molecular properties of the generated (blue), test set (grey), and randomly assembled (red) molecules. 2D properties includes: **a.** Molecular weight, **b.** LogP, **c.** QED, **d.** the number of hydrogen bond acceptors (HBA), **e.** the number of hydrogen bond donors, **f.** The number of rotatable bonds (ROT). 3D properties includes: **g.** The total amount of solvent accessible surface area (SASA), **h.** polar solvent accessible surface areas (PolarSASA), **i.** the radius of gyration.

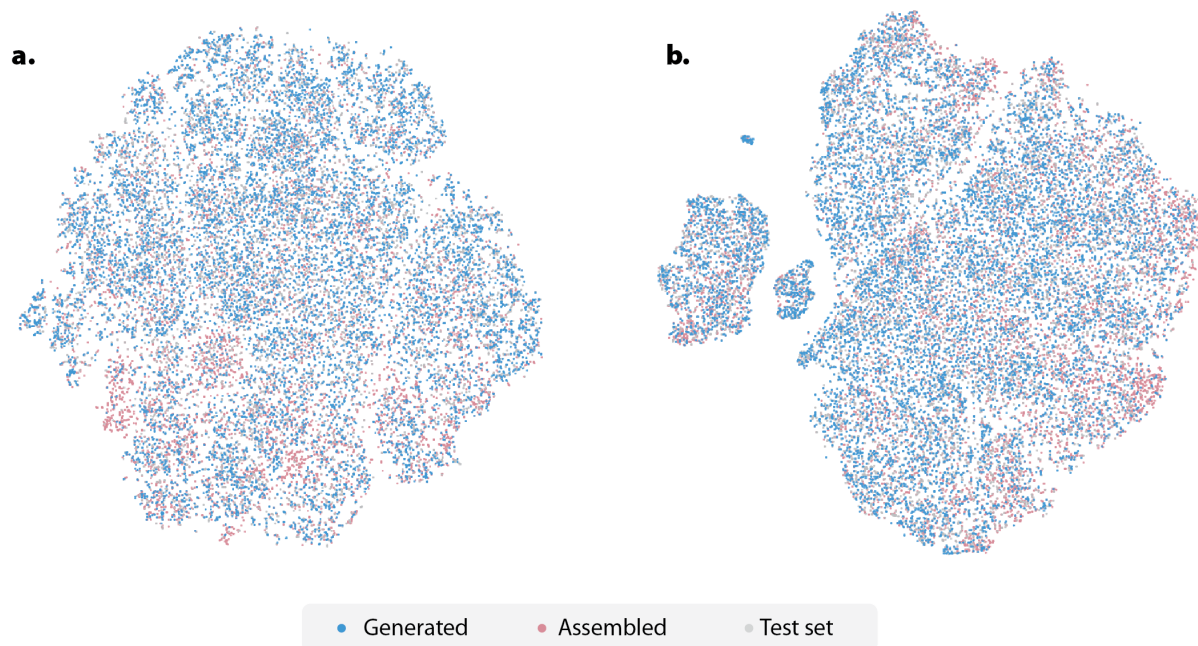


Figure S8: A t-SNE visualization of the distribution of **a.** Morgan fingerprint and **b.** USRCAT fingerprint. Blue dots represent generated molecules, grey dots represent test set molecules, and red dots represents molecules randomly assembled from the building blocks.

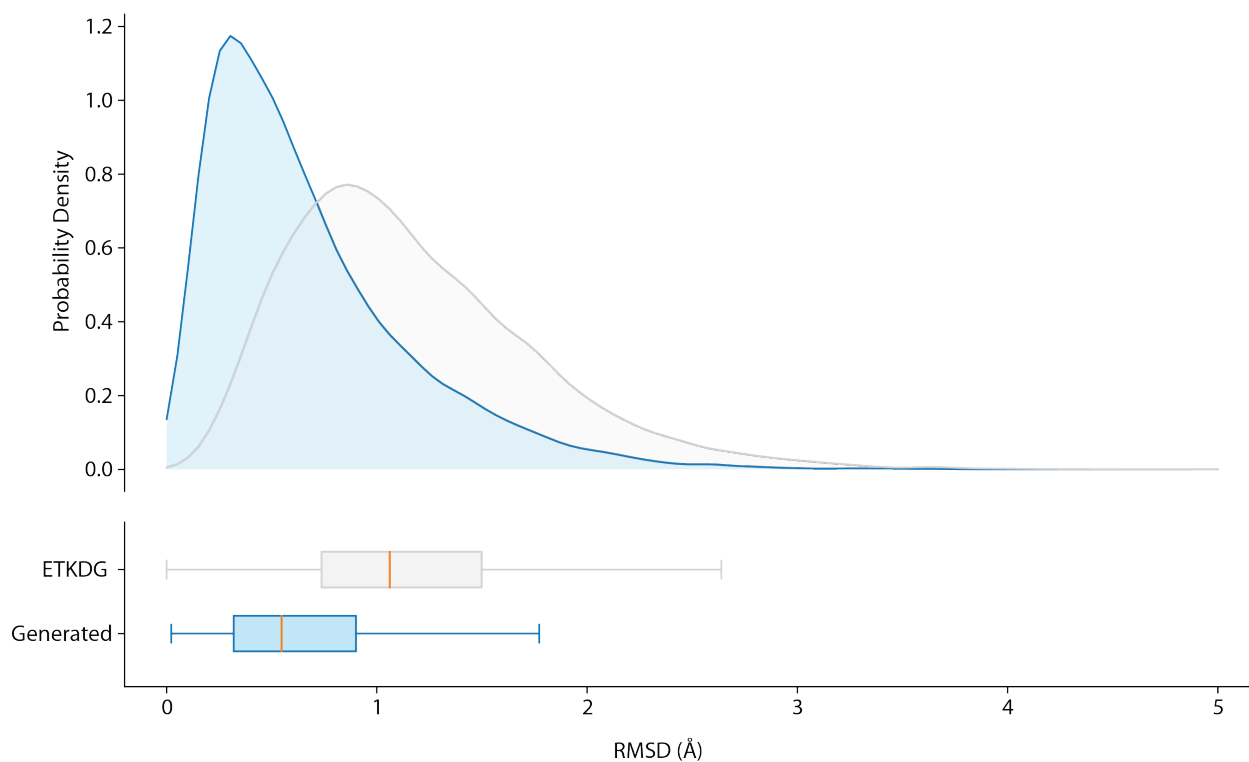


Figure S9: The distribution of RMSD values after relaxation with MMFF94s. Blue: molecules with conformations generated by the network. Grey: molecules with conformations generated by the ETKDG method provided by RDKit

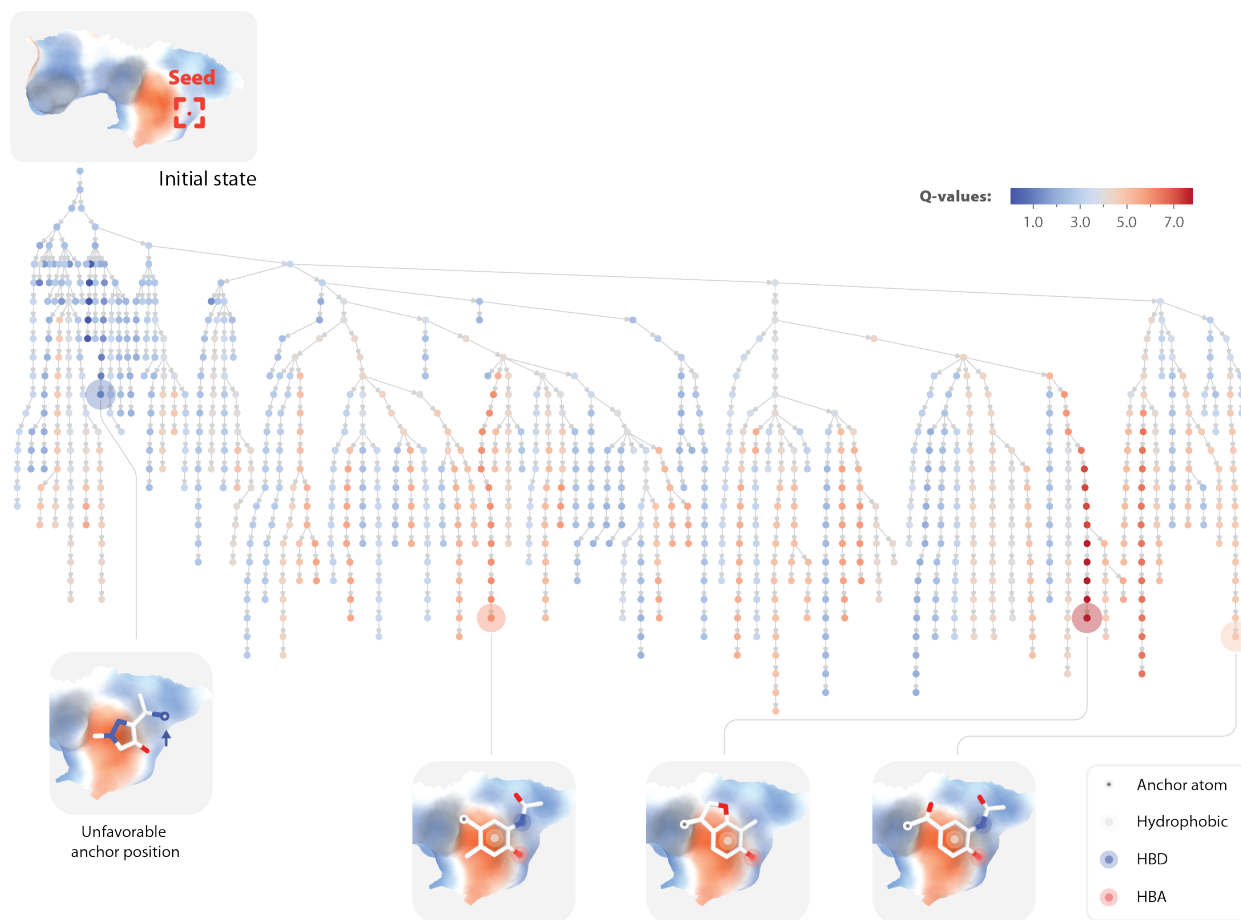


Figure S10: The detailed structure of the search tree for the first synthon in the BTK's ATP-binding pocket (only containing nodes with visit count larger than 25). Some generated synthon structures are shown below the tree, with important pharmacophore features highlighted. The leftmost example shows a state with a low estimated Q-value, which largely resulted from the unfavorable anchor position. As the result, this state is not as frequently visited as other states with higher Q-values.



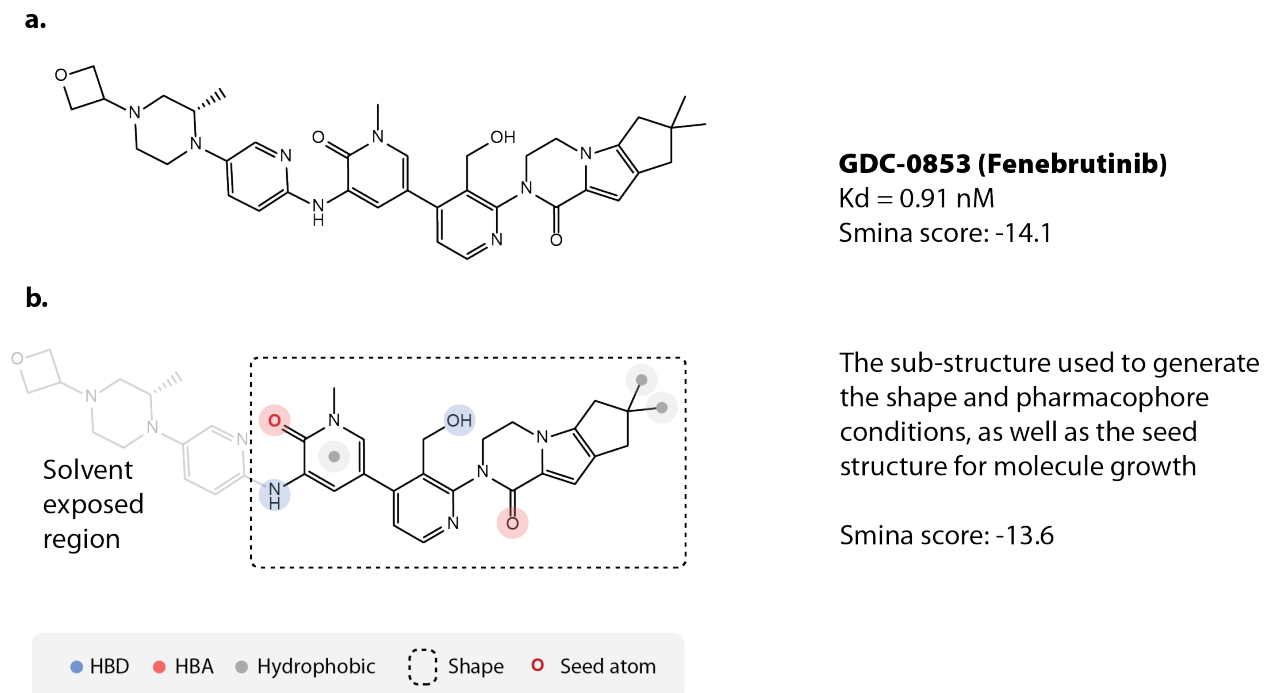


Figure S11: **a.** The topological structure of GDC-0853 (Fenebrutinib). **b.** The part of GDC-0853 used extract pharmacophore, shape, and seed for molecule generation. Note that some part of GDC-0853 inside the solvent-exposed region is not considered for pharmacophore and shape extraction.

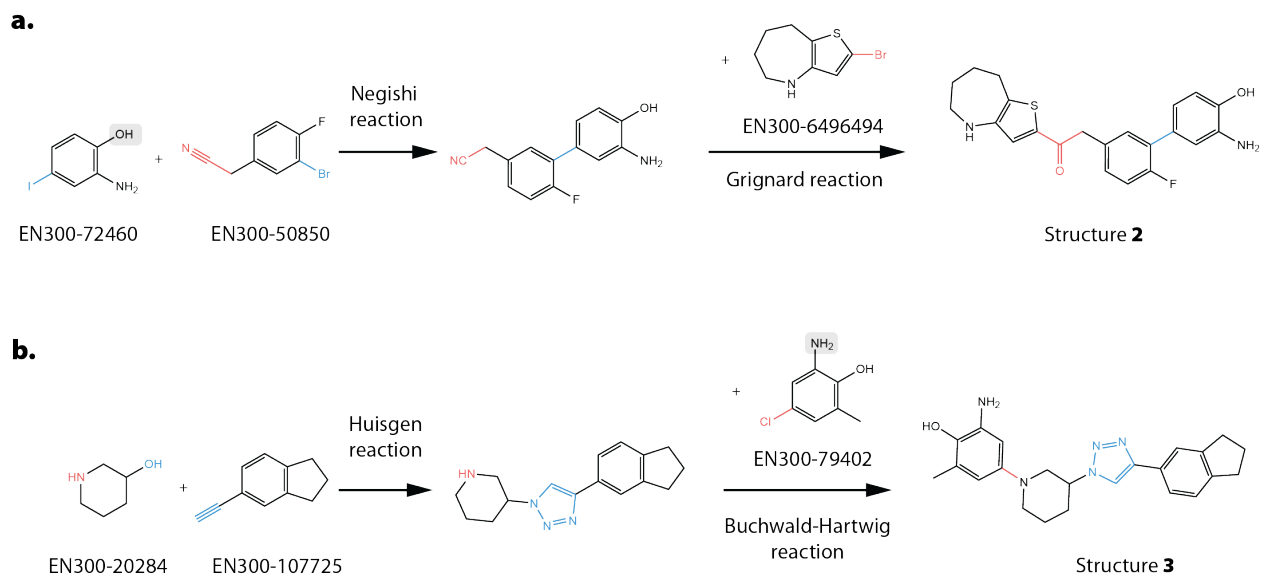


Figure S12: The proposed synthetic path for Structure 2 (**a**) and Structure 3 (**b**) by the model. Functional groups marked in grey needs to be protected before the reactions.

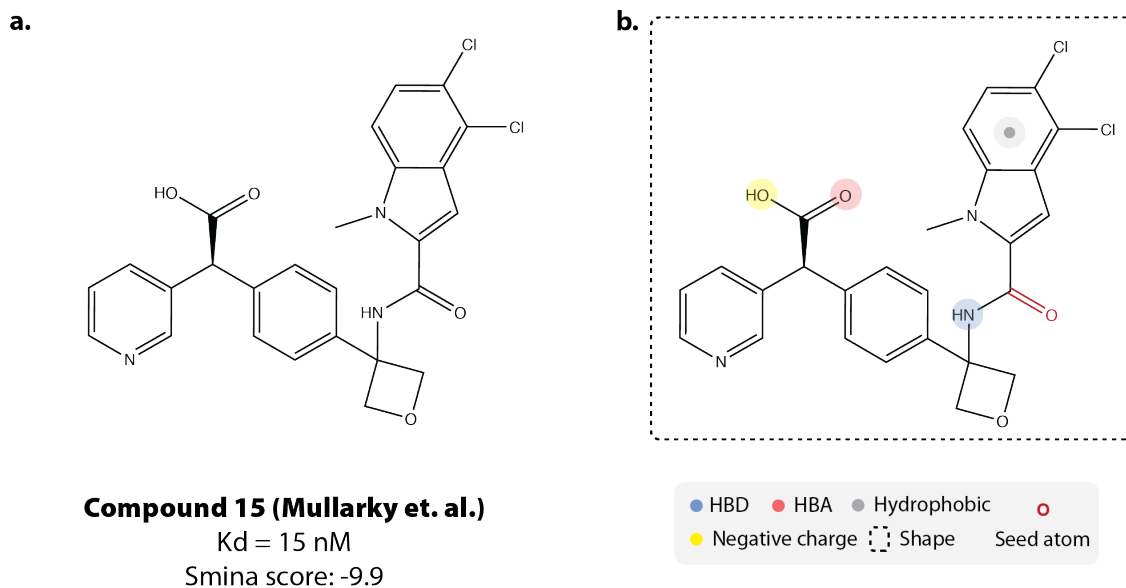


Figure S13: **a.** The topological structure of Compound 15, a potent inhibitor targeting the NAD pocket of PHGDH. **b.** The pharmacophore features extracted from the binding mode of the molecule, as well as the seed location for molecule growth.

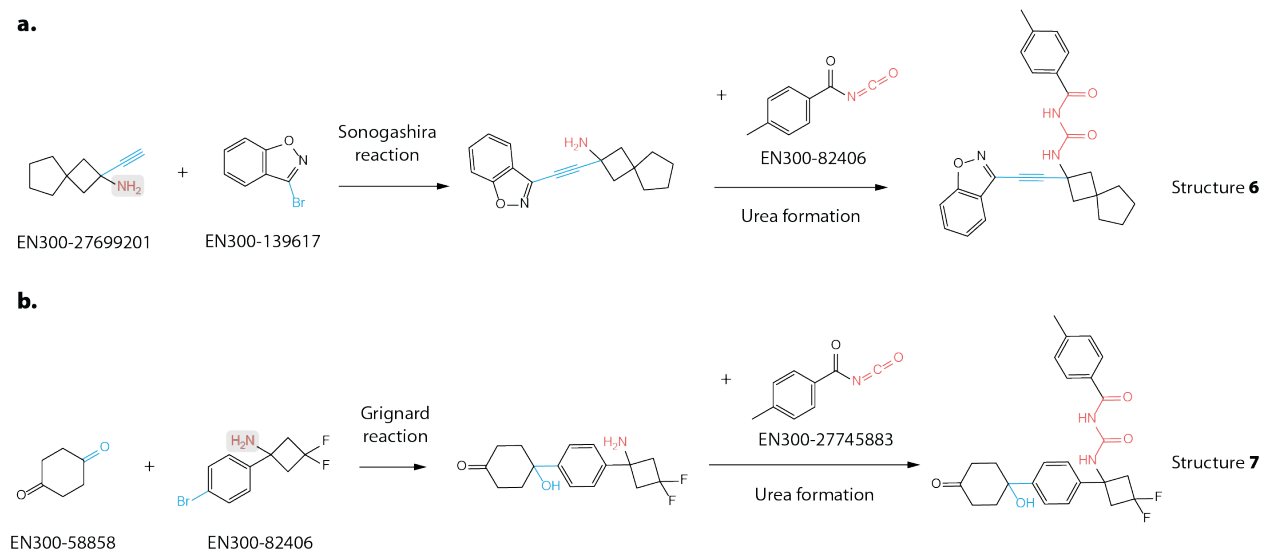


Figure S14: The proposed synthetic path for Structure 6 (**a**) and Structure 7 (**b**) by the model. Functional groups marked in grey needs to be protected before the reactions.

### 3 Supplementary tables

Table S1: A summary of different hyperparameter configurations experimented in this work (BBs: building blocks, LR: learning rate)

Group	Model architecture				Training parameter				Generation
	Variant name	IPA	3D pair embedding	Width ( $F$ )	DepthDecay frequency (#-steps)	Noise probability	Noise scale( $\text{\AA}$ )	Building block	
BBs	Default configuration	✓	✓	512	6	0.5	0.1	Global	
	EU stock	✓	✓	512	6	0.5	0.1	<b>EU</b>	
	Comprehensive catalog	✓	✓	512	6	0.5	0.1	<b>Comprehensive</b>	
3D encoding	Dropped IPA	×	✓	512	6	0.5	0.1	Global	
Scale	Dropped 3D pair embedding	✓	×	512	6	0.5	0.1	Global	
	Narrow network	✓	✓	<b>256</b>	6	0.5	0.1	Global	
LR	Shallow network	✓	✓	512	<b>3</b>	0.5	0.1	Global	
	Fast learning rate decay	✓	✓	512	6	<b>70</b>	0.1	Global	

	Model		Training			Generation		
	architecture		parameter	parameter	parameter	parameter		
Slow learning	✓	✓	512	6	<b>300</b>	0.5	0.1	Global
rate decay								
High noise	✓	✓	512	6	150	<b>0.9</b>	0.1	Global
probability								
Low noise	✓	✓	512	6	150	<b>0.1</b>	0.1	Global
probability								
High noise scale	✓	✓	512	6	150	0.5	<b>0.2</b>	Global
Low noise scale	✓	✓	512	6	150	0.5	<b>0.05</b>	Global

Table S2: The distribution of 2D molecular properties among molecules generated from models with different hyperparameters (see Table S1 for a detailed description of each configuration). We report the mean and standard deviation for each property, as well as the estimated Wasserstein distance to the test set. For the first row, we report the statistics of molecules randomly assembled from building blocks without any drug-likeness filtering.

Model variant	MW		LogP		HBA		HBD		ROT		QED							
	mean	std	wd	mean	std	wd	mean	std	wd	mean	std	wd						
Randomly assembled	454.32	47.45	35.46	3.48	1.37	0.57	6.81	1.64	0.7	1.91	1.12	0.33	6.96	2.22	0.93	0.45	0.15	0.18
Default configuration	412.31	42.39	7.64	2.9	1.2	0.12	6.13	1.54	0.08	1.69	0.98	0.08	6.05	1.85	0.12	0.62	0.12	0.03
EU stock	416.63	43.96	4.84	3.02	1.2	0.11	6.12	1.51	0.06	1.76	1.02	0.14	6.13	1.93	0.16	0.60	0.13	0.05
Comprehensive	415.46	42.65	4.85	2.91	1.21	0.13	6.15	1.51	0.05	1.73	0.99	0.1	6.12	1.86	0.09	0.62	0.12	0.03
catalog																		
Dropped IPA	413.22	42.51	6.82	2.94	1.19	0.09	6.07	1.51	0.08	1.69	0.97	0.07	6.07	1.86	0.12	0.62	0.12	0.03
Dropped 3D pair	414.91	41.63	4.93	2.93	1.16	0.07	6.11	1.5	0.05	1.66	0.97	0.05	6.07	1.82	0.08	0.62	0.11	0.03
embedding																		
Narrow network	411.01	42.46	8.91	2.95	1.2	0.1	6.04	1.52	0.11	1.68	0.98	0.07	6.03	1.86	0.14	0.62	0.12	0.04
Shallow network	412.79	42.25	7.14	2.93	1.2	0.11	6.1	1.52	0.07	1.69	0.98	0.08	6.06	1.88	0.13	0.62	0.12	0.03
Fast learning rate	411.36	42.44	8.57	2.94	1.19	0.1	6.06	1.54	0.11	1.7	0.98	0.08	6.03	1.89	0.16	0.62	0.12	0.04
decay																		
Slow learning rate	413.53	42.63	6.58	2.94	1.19	0.09	6.12	1.52	0.06	1.67	0.99	0.08	6.11	1.87	1.87	0.62	0.12	0.03
decay																		
High noise probability	414.14	41.36	5.61	2.94	1.17	0.07	6.09	1.5	0.06	1.69	0.99	0.08	6.07	1.82	0.09	0.62	0.12	0.03

Model variant	MW	LogP	HBA	HBD	ROT	QED													
Low noise probability	416.82	45.94	6.43	2.89	1.26	0.18	6.3	1.55	0.19	1.72	1.03	0.13	5.91	1.9	0.26	0.6	0.14	0.05	
Large noise scale	413.76	41.78	6.08	2.94	1.18	0.08	6.12	1.5	0.05	1.71	0.98	0.09	6.03	1.81	0.11	0.62	0.12	0.03	
Small noise scale	413.24	42.9	6.95	2.93	1.19	0.1	6.14	1.53	0.07	1.7	0.99	0.09	6.03	1.86	0.14	0.62	0.12	0.04	
Validation set	419.52	40.27	-	2.98	1.1	-	6.13	1.46	-	1.65	0.92	-	6.14	1.77	-	0.63	0.09	-	
Test set	419.72	40.13	-	2.97	1.11	-	6.14	1.46	-	1.46	0.92	-	6.14	1.77	-	0.62	0.09	-	
																			0.09

Table S3: The distribution of 3D molecular properties among molecules generated from models with different hyperparameters (see Table S1 for a detailed description of each configuration). We report the mean and standard deviation for each property, as well as the estimated Wasserstein distance to the test set. For the first row, we report the statistics of molecules randomly assembled from building blocks without any drug-likeness filtering.

Model variant	SASA			Polar SASA			Radius of gyration		
	mean	std	wd	mean	std	wd	mean	std	wd
Randomly assembled	667.72	60.84	41.41	185.77	58.93	26.24	4.9	0.71	0.3
Default configuration	617.86	53.27	10.07	162.93	49.92	2.96	4.56	0.63	0.05
EU stock	624.14	55.58	6.01	163.68	51.66	4.83	4.61	0.64	0.03
Comprehensive catalog	620.45	54.08	7.91	163.53	49.83	3.05	3.05	0.63	0.04
Dropped IPA	620.16	54.23	8.24	162.19	49.44	2.44	4.6	0.64	0.03
Dropped 3D pair embedding	621.13	52.84	6.8	161.87	49.19	2.24	4.59	0.62	0.02
Narrow network	618.08	53.9	10.04	161.95	49.53	2.56	4.59	0.64	0.03
Shallow network	619.66	54.05	8.62	162.59	50.19	3.19	4.6	0.63	0.02
Fast learning rate decay	616.74	53.97	11.34	161.7	49.55	2.63	4.58	0.64	0.04
Slow learning rate decay	619.5	53.42	8.54	162.15	50.4	3.41	4.57	0.63	0.05
High noise probability	620.89	52.67	6.99	162.3	49.31	2.3	4.6	0.63	0.02
Low noise probability	614.44	56.41	14.35	166.52	52.61	6.96	4.47	0.6	0.15
Large noise scale	619.44	52.9	8.45	162.75	50.11	3.12	4.59	0.63	0.03
Small noise scale	618.84	54.05	9.38	162.16	49.65	2.65	4.57	0.63	0.05
Validation set	627.61	50.87	-	162.5	47.12	-	4.62	0.62	-

Model variant	SASA	Polar SASA	Radius of gyration
Test set	627.52	162.57	4.61
	50.49	46.89	0.61
	-	-	-



Table S4: Quantitative measurement of the quality of generated samples. The first two columns indicate the sample diversity measured using Tanimoto and USRCAT fingerprints. The third and fourth column shows the 2D and 3D MMD values, which measures the ability of the network to correctly model the distribution in the chemical space. The final column contains the average RMSD after conformers are relaxed using MMFF94s forcefield. Each row represents a different hyperparameter configuration, as detailed in Table S1. The first row represents molecules randomly assembled from building blocks without any drug-likeness filtering.

Model variant	Diversity(2D)	Diversity(3D)	MMD(2D)	MMD(3D)	Mean RMSD(Å)
Randomly assembled	0.120	0.156	0.003604	0.003492	1.142 (ETKDG)
Default configuration	0.121	0.162	0.000158	0.000156	0.692
EU stock	<b>0.123</b>	0.161	0.000798	0.000109	0.725
Comprehensive catalog	0.121	0.162	0.000134	0.000122	0.691
Dropped IPA	0.121	0.161	0.000195	0.000068	0.696
Dropped 3D pair embedding	0.122	0.162	<b>0.000082</b>	<b>0.000045</b>	0.718
Narrow network	0.121	0.161	0.000256	0.000066	0.716
Shallow network	0.121	0.161	0.000204	0.000059	0.707
Fast learning rate decay	0.121	0.161	0.000224	0.000126	0.734
Slow learning rate decay	0.121	0.162	0.000183	0.000120	<b>0.672</b>
High noise probability	0.122	0.162	0.000171	0.000060	0.685
Low noise probability	0.120	<b>0.165</b>	0.000475	0.000954	0.795
Large noise scale	0.122	0.162	0.000163	0.000080	0.685
Small noise scale	0.121	0.162	0.000212	0.000143	0.713

## References

- (S1) Hartenfeller, M.; Eberle, M.; Meier, P.; Nieto-Oberhuber, C.; Altmann, K.-H.; Schneider, G.; Jacoby, E.; Renner, S. A Collection of Robust Organic Synthesis Reactions for In Silico Molecule Design. *Journal of Chemical Information and Modeling* **2011**, *51*, 3093–3098.
- (S2) Goldberg, F. W.; Kettle, J. G.; Kogej, T.; Perry, M. W.; Tomkinson, N. P. Designing novel building blocks is an overlooked strategy to improve compound quality. *Drug Discovery Today* **2015**, *20*, 11–17.
- (S3) London, N.; Miller, R. M.; Krishnan, S.; Uchida, K.; Irwin, J. J.; Eidam, O.; Gibbold, L.; Cimermančič, P.; Bonnet, R.; Shoichet, B. K.; Taunton, J. Covalent docking of large libraries for the discovery of chemical probes. *Nature Chemical Biology* **2014**, *10*, 1066–1072.
- (S4) Li, Y.; Pei, J.; Lai, L. Structure-based de novo drug design using 3D deep generative models. *Chemical Science* **2021**, *12*, 13664–13675.
- (S5) Ahn, S.; Chen, B.; Wang, T.; Song, L. Spanning tree-based graph generation for molecules. International Conference on Learning Representations.
- (S6) Li, Y.; Zhang, L.; Liu, Z. Multi-objective de novo drug design with conditional graph generative model. *Journal of Cheminformatics* **2018**, *10*, 33.
- (S7) Powers, A. S.; Yu, H. H.; Suriana, P.; Dror, R. O. Fragment-Based Ligand Generation Guided By Geometric Deep Learning On Protein-Ligand Structure. *bioRxiv* **2022**, 2022.03.17.484653.
- (S8) Adams, K.; Coley, C. W. Equivariant Shape-Conditioned Generation of 3D Molecules for Ligand-Based Drug Design. *arXiv* **2022**,

- (S9) Taminau, J.; Thijs, G.; Winter, H. D. Pharaos: Pharmacophore alignment and optimization. *Journal of Molecular Graphics and Modelling* **2008**, *27*, 161–169.
- (S10) Kurkinen, S. T.; Lätti, S.; Pentikäinen, O. T.; Postila, P. A. Getting Docking into Shape Using Negative Image-Based Rescoring. *Journal of Chemical Information and Modeling* **2019**, *59*, 3584–3599.
- (S11) Skalic, M.; Jiméenez, J.; Sabbadin, D.; Fabritiis, G. D. Shape-Based Generative Modeling for de Novo Drug Design. *Journal of Chemical Information and Modeling* **2019**, *59*, 1205–1214.
- (S12) Grant, J. A.; Gallardo, M.; Pickup, B. T. A fast method of molecular shape comparison: A simple application of a Gaussian description of molecular shape. *Journal of computational chemistry* **1996**, *17*, 1653–1666.
- (S13) Wang, Q.; Birod, K.; Angioni, C.; Grösch, S.; Geppert, T.; Schneider, P.; Rupp, M.; Schneider, G. Spherical Harmonics Coefficients for Ligand-Based Virtual Screening of Cyclooxygenase Inhibitors. *PLoS ONE* **2011**, *6*, e21554.
- (S14) Ivanic, J.; Ruedenberg, K. Rotation Matrices for Real Spherical Harmonics. Direct Determination by Recursion. *The Journal of Physical Chemistry A* **1998**, *102*, 9099–9100.
- (S15) Vaswani, A.; Shazeer, N.; Parmar, N.; Uszkoreit, J.; Jones, L.; Gomez, A. N.; Kaiser, L.; Polosukhin, I. Attention Is All You Need. *arXiv* **2017**,
- (S16) Jumper, J.; Evans, R.; Pritzel, A.; Green, T.; Figurnov, M.; Ronneberger, O.; Tunyasuvunakool, K.; Bates, R.; Žídek, A.; Potapenko, A.; Bridgland, A.; Meyer, C.; Kohl, S. A. A.; Ballard, A. J.; Cowie, A.; Romera-Paredes, B.; Nikolov, S.; Jain, R.; Adler, J.; Back, T.; Petersen, S.; Reiman, D.; Clancy, E.; Zielinski, M.; Steinegger, M.; Pacholska, M.; Berghammer, T.; Bodenstern, S.; Silver, D.; Vinyals, O.; Senior, A. W.;

- Kavukcuoglu, K.; Kohli, P.; Hassabis, D. Highly accurate protein structure prediction with AlphaFold. *Nature* **2021**, *596*, 583–589.
- (S17) Ba, J. L.; Kiros, J. R.; Hinton, G. E. Layer Normalization. *arXiv* **2016**,
- (S18) Clevert, D.-A.; Unterthiner, T.; Hochreiter, S. Fast and Accurate Deep Network Learning by Exponential Linear Units (ELUs). *arXiv* **2015**,
- (S19) Lipinski, C. A.; Lombardo, F.; Dominy, B. W.; Feeney, P. J. Experimental and computational approaches to estimate solubility and permeability in drug discovery and development settings1PII of original article: S0169-409X(96)00423-1. The article was originally published in *Advanced Drug Delivery Reviews* 23 (1997) 3–25.1. *Advanced Drug Delivery Reviews* **2001**, *46*, 3–26.
- (S20) Veber, D. F.; Johnson, S. R.; Cheng, H.-Y.; Smith, B. R.; Ward, K. W.; Kopple, K. D. Molecular Properties That Influence the Oral Bioavailability of Drug Candidates. *Journal of Medicinal Chemistry* **2002**, *45*, 2615–2623.
- (S21) Baell, J.; Walters, M. A. Chemistry: Chemical con artists foil drug discovery. *Nature* **2014**, *513*, 481–483.
- (S22) Bickerton, G. R.; Paolini, G. V.; Besnard, J.; Muresan, S.; Hopkins, A. L. Quantifying the chemical beauty of drugs. *Nature Chemistry* **2012**, *4*, 90–98.
- (S23) Kingma, D. P.; Ba, J. Adam: A Method for Stochastic Optimization. *arXiv* **2014**, <https://arxiv.org/abs/1412.6980>.
- (S24) Wang, R.; Fang, X.; Lu, Y.; Wang, S. The PDBbind Database: Collection of Binding Affinities for Protein-Ligand Complexes with Known Three-Dimensional Structures. *Journal of Medicinal Chemistry* **2004**, *47*, 2977–2980.

- (S25) Xiao, C.; Huang, R.; Mei, J.; Schuurmans, D.; Muller, M. Maximum entropy monte-carlo planning. *Advances in Neural Information Processing Systems* **2019**, *32*, 9520–9528.
- (S26) Chaslot, G. M. J. B.; Winands, M. H. M.; Herik, H. J. v. d. Parallel Monte-Carlo tree search. *Proceedings of 6th International Conference on Computers and Games (CG)* **2008**, *5131*, 60–71.
- (S27) Gretton, A.; Borgwardt, K. M.; Rasch, M. J.; Scholkopf, B.; Smola, A. A kernel two-sample test. *The Journal of Machine Learning Research* **2012**, *13*, 723–773.
- (S28) Li, Y.; Hu, J.; Wang, Y.; Zhou, J.; Zhang, L.; Liu, Z. DeepScaffold: A Comprehensive Tool for Scaffold-Based De Novo Drug Discovery Using Deep Learning. *Journal of Chemical Information and Modeling* **2019**, *60*, 77–91.
- (S29) Schärfer, C.; Schulz-Gasch, T.; Ehrlich, H.-C.; Guba, W.; Rarey, M.; Stahl, M. Torsion Angle Preferences in Druglike Chemical Space: A Comprehensive Guide. *Journal of Medicinal Chemistry* **2013**, *56*, 2016–2028.
- (S30) Riniker, S.; Landrum, G. A. Better Informed Distance Geometry: Using What We Know To Improve Conformation Generation. *Journal of Chemical Information and Modeling* **2015**, *55*, 2562–2574.